A modular framework for multiscale, multicellular, spatiotemporal modeling of acute primary viral infection and immune response in epithelial tissues and its application to drug therapy timing and effectiveness

A multiscale model of viral infection in epithelial tissues

T.J. Sego[1,2*], Josua O. Aponte-Serrano[1,2*], Juliano Ferrari Gianlupi[1,2], Samuel R. Heaps[1], Kira Breithaupt[1,3], Lutz Brusch[4], James M. Osborne[5], Ellen M. Quardokus[1], Richard K. Plemper[6], James A. Glazier[1,2]

[1] Department of Intelligent Systems Engineering, Indiana University, Bloomington, IN, USA
[2] Biocomplexity Institute, Indiana University, Bloomington, IN, USA
[3] Cognitive Science Program, Indiana University, Bloomington, IN, USA
[4] Center for Information Services and High Performance Computing (ZIH), Technische Universität Dresden, Germany
[5] School of Mathematics and Statistics, University of Melbourne, Melbourne, 3010, Australia
[6] Institute for Biomedical Sciences, Georgia State University, Atlanta, GA, USA
[*] These Authors contributed equally to this study

Abstract

Simulations of tissue-specific effects of primary acute viral infections like COVID-19 are essential for understanding differences in disease outcomes and optimizing therapeutic interventions. We present a multiscale model and simulation of an epithelial tissue infected by a virus, a simplified cellular immune response and viral and immune-induced tissue damage. The model exhibits basic patterns of infection dynamics: widespread infection, slowed infection, recurrence, containment and clearance. Inhibition of viral internalization and faster immune-cell recruitment promote containment of infection. Fast viral internalization and slower immune response lead to uncontrolled spread of infection. Because antiviral drugs can have side effects at high doses and show reduced clinical effectiveness when given later during the course of infection, we studied the effects on infection progression of both treatment potency (which combines drug effectiveness and dosage) and time-of-first treatment after infection. Simulation of a drug which reduces the replication rate of viral RNA shows that even a low potency therapy

greatly decreases the total tissue damage and virus burden when given near the beginning of infection. However, even a high potency therapy rapidly loses effectiveness when given later near the time of peak viral load in the untreated case. Many combinations of dosage and treatment time lead to stochastic outcomes, with some simulation replicas showing clearance or control of the virus (treatment success), while others show rapid infection of all epithelial cells in the simulated tissue subregion (treatment failure). This switch between a regime of consistent treatment success and failure occurs as the time of treatment increases. However, stochastic variations in viral spread mean that high potency treatments at late times are occasionally effective. The model is open-source and modular, allowing rapid development and extension of its components by groups working in parallel.

Author summary

This study presents an open source multiscale model of viral immune interactions in epithelial tissues. The model is used to investigate how potential treatments influence the simulation outcome. Simulation results suggest that drugs that interfere with virus replication (*e.g.*, remdesivir) yield substantially improved infection outcomes when administered prophylactically even at very low doses than when used at high doses as treatment for an infection that has already begun.

Introduction

The current global pandemic of COVID-19, caused by the novel coronavirus Severe Acute Respiratory Syndrome Coronavirus 2 (SARS-CoV-2), has motivated the study of beta coronavirus diseases at different spatial and temporal scales [1]. The time course, severity of symptoms and complications from SARS-CoV-2 infection are highly variable from patient to patient [2]. Mathematical modeling methods to integrate the available host- and pathogen-level data on disease dynamics are required to apply them effectively to research into therapeutic interventions [3–5]. Spatial model development of beta coronaviruses that incorporate the dynamics at these different levels and scales is emerging [6,7].

Mathematical models and computer simulations have been extensively used to study in-host progression of viral infection [8]. Building multiscale models of acute primary viral infection requires interdisciplinary collaboration to design model structures that integrate different scales and different biological components (e.g., viral replication and internalization, immune system responses). To build a model of COVID-19 or other viral infections, we need to consider some aspects of the virus replication life cycle, the time course of infection, virus spread in tissue, and host mediated effects of the immune response. Higher-level comprehensive models simplify aspects of infection but model multiple mechanisms and phases of disease progression (*e.g.*, combined models of viral infection and age-dependent immune response [9]). Non-spatial kinetic approaches are commonly used to model different stages of the viral replication cycle, such as binding and internalization [10,11], viral genome replication and translation [12,13], assembly, packaging and release [14,15].

Virus families are classified by their genome type and replication cycle [16]. Specialized models have been developed for many virus families: positive-sense single-stranded RNA viruses such as hepatitis C virus, poliovirus and Semliki Forest virus [10,17,18], negative single-stranded RNA viruses such as influenza A [19,20], single-stranded RNA retroviruses such as human immunodeficiency virus (HIV) [21,22], double-stranded DNA viruses such as herpes simplex virus [23] and double-stranded DNA retroviruses such as hepatitis virus B [24]. Non-spatial models average over spatio-temporal and multicellular variation and may not reflect the effects of tissue heterogeneity (*e.g.*, when the infection starts from a few widely scattered infected cells [25]). Spatially-resolved models of infection include cellular automata [26], partial differential equations [27] and fluid-dynamic models [28]. The disease progression of HIV [27,29–32] and the dissemination of influenza virus to the lower respiratory tract [33,34] have been modeled using agent-based spatial approaches.

In this paper, we will consider acute primary infection, infection by a virus which the immune system has not previously encountered, that causes a disease of relatively rapid onset and short duration where a properly functioning immune system eventually eliminates the virus completely (clearance) and symptoms range from mild to severe. While the details of infection vary by virus and patient, infection generally begins when a limited number of target cells in one or more tissues are exposed to and internalize the virus. The virus begins to replicate within the initially infected target cells, but cells do not release any newly synthesized virus for a period of hours to days (the eclipse or lag phase of the infection). Infected cells release proinflammatory cytokines and complement proteins as a warning to neighboring cells [35,36]. Some of these cytokines, like Type 1 interferons, can induce autocrine and paracrine responses to the virus (*e.g.*, inhibiting viral replication, viral entry or even cell death) [37]. Cytokines attract immune cells within the tissue by chemotaxis and recruit circulating immune cells from the blood. Immune cells targeted by early activation of the innate immune response are dendritic cells, macrophages, neutrophils, mast cells, basophils, eosinophils, leukocytes, and natural killer (*NK*) cells [38]. Some of these immune cells themselves release both pro- and anti-inflammatory signals. Phagocytosis by resident and recruited macrophages and neutrophils (which begins even before viral entry) is maximal in strength during the first two days after the initial infection, modulating the amount of extracellular virus. These signals also activate cytotoxic innate immune cells like NK cells within the tissue, which kill infected cells. Once infected cells begin to release virus, the amount of extracellular virus increases exponentially over a period of a few days, reaching a peak fairly early during infection. As the viral load increases, immune signaling increases rapidly (this increase is associated with the onset of fever and other symptoms) recruiting more circulating cells of the innate immune system to the infection site. Over the next few days, in response to induced antiviral resistance, cell death and innate immune-cell activity, viral loads generally decrease.

Immune signals from the infected and innate immune cells help trigger the adaptive immune response. Macrophages and dendritic cells that have engulfed and degraded viral pathogens or fragments of dead infected cells travel to nearby lymph nodes and serve as viral

antigen presenting cells (*APC*s) to naive T-cells. Antigen presentation induces naive T cell proliferation and differentiation into pathogen-specific memory and effector T cells. Effector T cells migrate to the site of infection and induce apoptosis of infected cells by antigen recognition. In acute infections, adaptive immune response leads to pathogen neutralization and clearance [39]. Viral loads usually decrease rapidly as adaptive immune cells like CD8+ T-cells enter the tissue and eliminate infected cells. Cells also begin to send out anti-inflammatory signals, shutting down the immune response as viral clearance proceeds. Antigen presentation within the immune system also induces activation of naive B-cell lymphocytes into antibody-producing memory B-cells and plasma cells. The adaptive immune response remembers its exposure to previous pathogens and provides the body with pathogen-specific effector cells and antibodies which neutralize and clear them, providing long term immunity [40]. Tissue damage results from virus and cytokine-induced cell death (which is first noticeable after 2 or 3 days) and from killing of infected and uninfected cells by immune cells, which increases steadily until the end of viral clearance (7-10 days). Tissue recovery and healing start around the time of viral clearance and may last for several weeks.

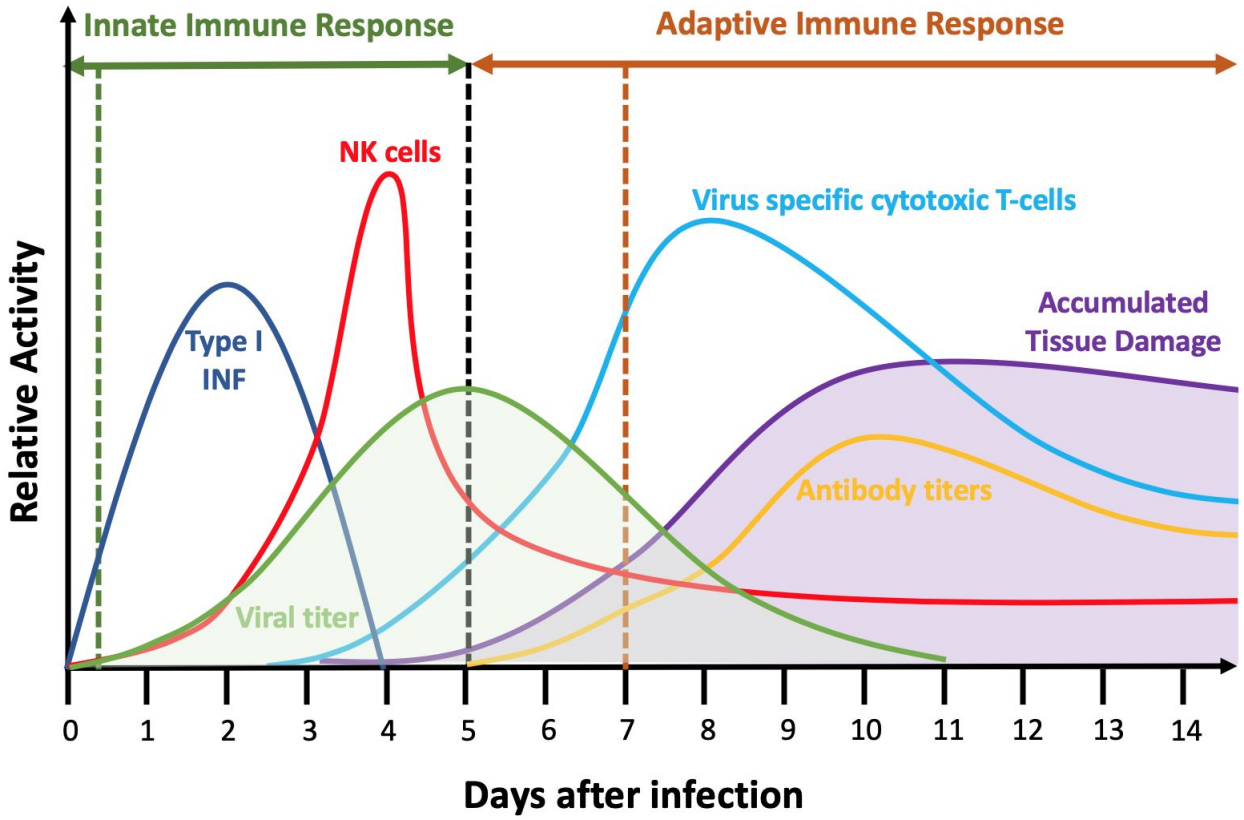

Figure 1: Innate and adaptive immune response time course indicated above graphs during the course of primary acute viral infection. From time 0 to the vertical green dotted line is when phagocytic cells engulf extracellular virus. Relative levels of Type I interferons (IFN) (dark blue), Natural Killer (NK) cells (red). The black vertical dotted line denotes the transition between innate and adaptive immune responses. Virus-specific cytotoxic T-cells (light blue) rise during the cell-mediated part of the adaptive immune response. The orange vertical dotted line denotes when the humoral part of the adaptive immune response begins with rising virus-specific antibody titers (orange). Viral

replication titers (shaded green curve) and accumulated tissue damage (shaded purple curve) in host epithelial tissue for an acute primary infection (Adapted from [41,42]).

In this work we developed a multiscale multicellular spatiotemporal model of the complex processes of infection and immune response in a tissue, focusing on viral replication and spread, the innate immune response and the earliest phases of the adaptive immune response. Our model consists of three interconnected components (Figure 2A): an epithelium component, an extracellular environment component and a lymph node component. The epithelium is represented as a compact monolayer of immobile epithelial cells that are classified by their current state of viral infection (*i.e.*, uninfected, infected, virus releasing, dead, Figure 2C). The extracellular environment is represented as a space above the epithelium and provides the space to which immune cells are recruited to and move, and into which viruses and chemicals are released. The chemicals and viruses released into the extracellular environment are represented by diffusive and decaying fields. Our generic immune cells represent a subset of the many types of tissue-localized immune cells moving in the extracellular environment. Together, the epithelium and the extracellular environment represent a patch of epithelial tissue (Figure 2A). The Lymph node component responds to the extracellular cytokine field by adding immune cells to the extracellular space when in a proinflammatory state and removing them when in an anti-inflammatory state. See the *Models and methods* section for details.

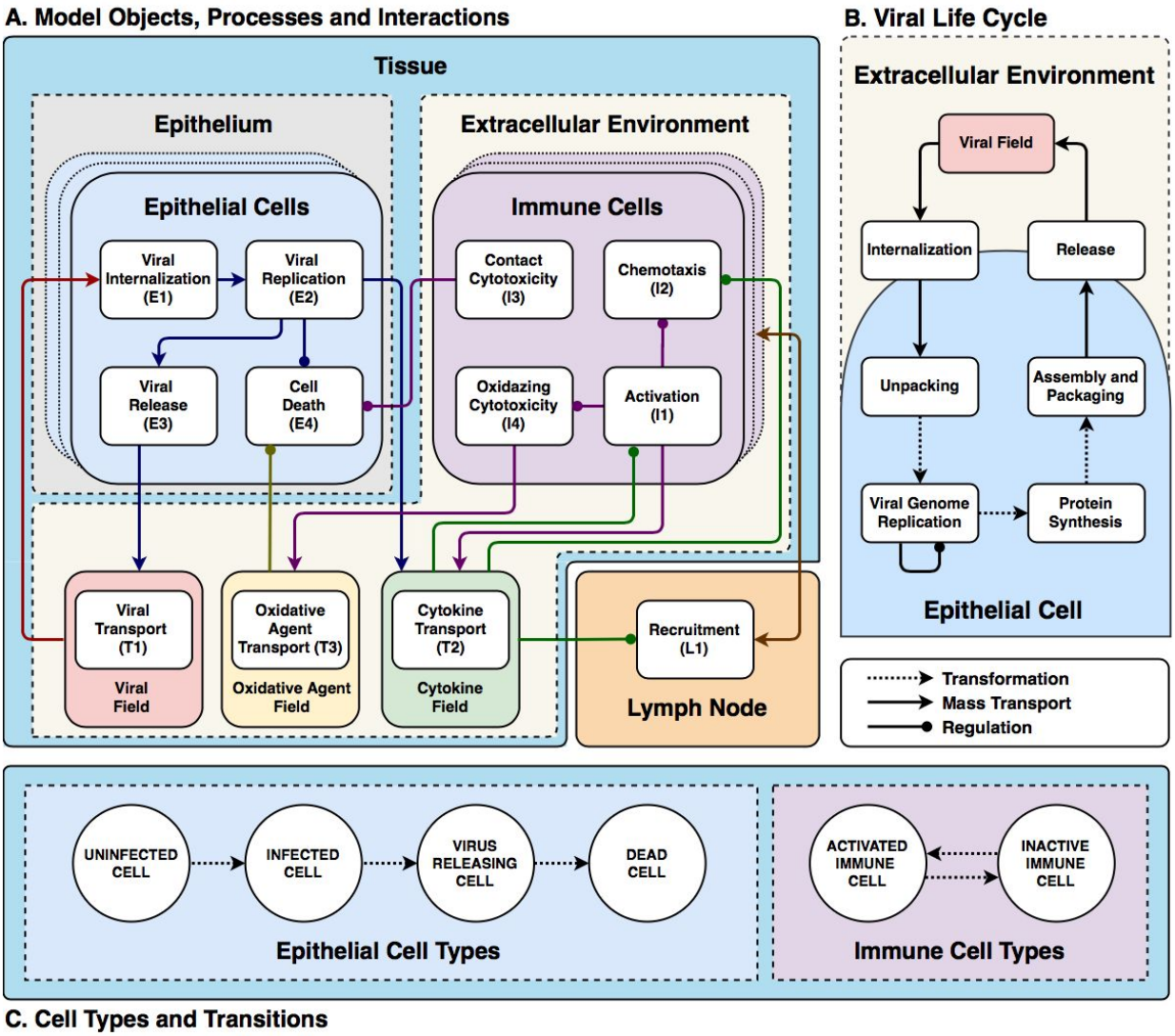

Figure 2. A. Model objects, processes and interactions: Conceptual model of a tissue and lymph node. Schematic representation of the model objects, processes and interactions in our model. Epithelial and immune cells refer to the two main classes of cells. Interactions occur within an extracellular environment, and a compartmental model of a lymph node controls immune-cell recruitment to the tissue. Together the epithelial-cell, extracellular-environment and immune-cell components represent the epithelial tissue. Each model object has associated processes that dictate its states and behaviors. Epithelial-cell processes include viral internalization (**E1**), viral replication (**E2**), viral release (**E3**) and cell death (**E4**). Immune cell processes include activation (**I1**), chemotaxis (**I2**), contact cytotoxicity (**I3**) and oxidative cytotoxicity (**I4**). *Activated* immune cells participate in oxidative cytotoxicity (**I4**) and secrete oxidative agents into the oxidizing-agent field (**T3**). Activated cells become inactive after 1 hour. The virus field (**T1**), cytokine field (**T2**) and oxidizing-agent field (**T3**) describe spatially-varying densities of extracellular components. Field processes describe diffusive transport and clearance of material in the extracellular environment and activated transport to the lymph nodes. The lymph node is a single-compartment model whose pro- or anti-inflammatory state specifies the recruitment or removal (**L1**) of immune cells in the epithelial tissue. The transport of cytokines to the lymph node promotes its proinflammatory state. **B. Viral Life Cycle: Interactions in the viral internalisation, replication and release models**. Schematic representation of inputs, outputs and interactions between stages of the viral replication model. Extracellular viral particles are internalized by the viral internalization model and initiate the viral replication model. The main stages of the viral replication model are: unpacking, viral genome replication, protein synthesis and viral assembly and packaging (U, R, P, and A). The output of the viral

replication model is passed to the viral release model, where newly assembled viral particles are released into the extracellular environment. **C. Cell types and transitions.** Epithelial cells are of type *uninfected* if they have not yet internalized any virus (**E1**). They are of type *infected* if they have internalized virus, but are not releasing virus into the virus field (viral release **E3** is inactive). They are of type *virus releasing* if they are releasing virus into the extracellular virus field (*i.e.*, viral release **E3** is activated). Immune cells are initially *inactive* and do not participate in the oxidative cytotoxicity (**I4**) or chemotax towards higher concentrations of the cytokine field (**I2**). They become *activated* when they experience activation (**I1**). In all panels, dashed arrows with barbed heads represent transformations, solid arrows with barbed heads represent transport and solid arrows with lollipop heads represent regulation.

We simulate extracellular-virus particle transport and clearance as continuous diffusion and decay. We approximate the discrete process of a cell's internalization of a virus particle by a stochastic virus internalization event (**E1**) determined by time elapsed, the local concentration of the virus field, and the number of available cell-surface receptors on the cell. We simplify the complexity of viral replication into four steps: unpacking, viral genome replication, protein synthesis and packaging/assembly (**E2**, Figure 2B) [6,18,43,44]. The subcellular kinetics of viral replication determine the rate of release of new viral particles into the extracellular environment, which contributes to furthering the spread of the virus in the tissue (**E3**). To represent the combined effect of the many types of virus-induced cell death, each infected epithelial cell has a probability of dying that depends on the number of assembled viral particles inside the cell per time (**E4**).

We simplify the complex biochemistry of many molecular signals like chemokines, interferons and viral fragments as a single generic extracellular cytokine field that acts both as a tissue-local and systemic inflammatory signal. Cytokine is secreted by infected epithelial cells and immune cells (**T2**). The cytokine field produces local immune effects such as activation (**I1**) and chemotaxis (**I2**) of immune cells. Activated immune cells can revert back to inactive immune cells when the cytokine signal ceases. The cytokine field also recruits immune cells to the tissue through long-distance signaling via the lymphatic system (**L1**). We model recruitment of immune cells to the simulation domain using an ordinary differential equation of the *immune signal* (S), which represents the balance between pro- and anti-inflammatory signaling, delay from transport through the lymphatic system and a resident immune cell population. Immune cells can cause epithelial cell death (**E4**) by three mechanisms. Immune cells kill infected epithelial cells by contact cytotoxicity, in which case neighboring epithelial cells can also die through a bystander effect (**I3**). In conditions with high cytokine levels, immune cells secrete a diffusive oxidative agent (**T3**) that kills uninfected, infected and virus-releasing epithelial cells (**I4**).

Results

We begin by presenting our base multicellular model of viral infection in an epithelial tissue, along with a simulation for a baseline set of parameters and basic analyses. We then explore the simulation's dependence on critical parameters that are important to understand acute primary viral infections of airway epithelial cells. All simulations and spatial, population and system-level metrics presented in this section follow the specifications in *Simulation*

Specifications. Simulations were performed using CompuCell3D [45]. Supplemental Information *Downloading and running the simulation* provides instructions on how to run simulations.

We initialize the simulations with periodic boundary conditions parallel to the plane of the sheet and Neumann boundary conditions perpendicular to the plane of the sheet. Initially, the extracellular environment does not contain any extracellular virus, cytokines, oxidative agents or immune cells. We introduce infection by creating a single infected epithelial cell at the center of the epithelial sheet. To illustrate the full range of dynamics of viral infection in the presence of an immune response, we established a baseline set of parameters (Table 1) for which the immune response is strong enough to slow the spread of the infection, but insufficient to prevent widespread infection and death of all epithelial cells (Figure 3).

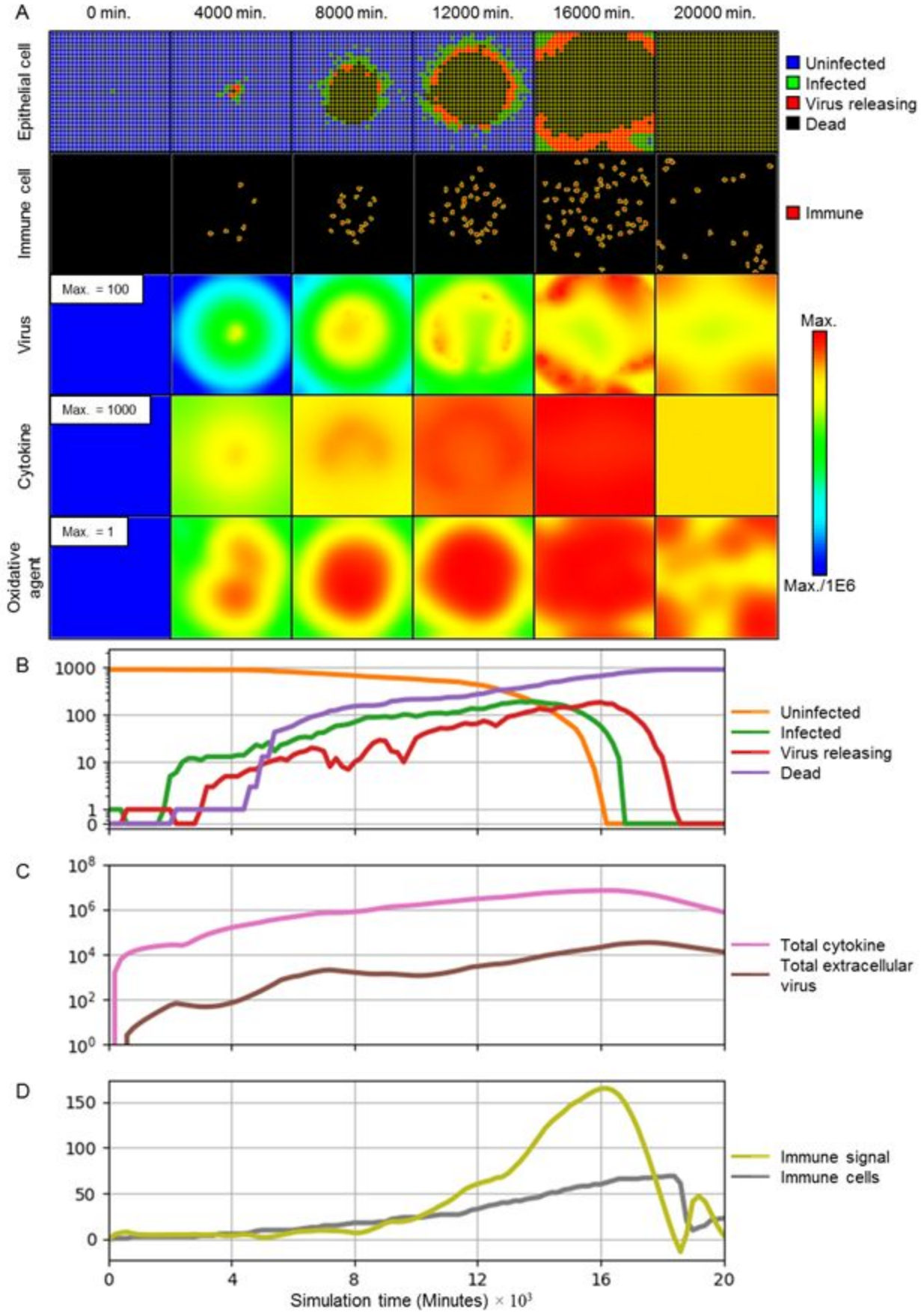
A
0 min.
4000 min.
8000 min.
12000 min.
16000 min.
20000 min.
Epithelial cell
Immune cell
Virus
Cytokine
Oxidative agent
Max. = 100
Max. = 1000
Max. = 1
Uninfected
Infected
Virus releasing
Dead
Immune
Max.
Max./1E6
B
Uninfected
Infected
Virus releasing
Dead
C
Total cytokine
Total extracellular virus
D
Immune signal
Immune cells
Simulation time (Minutes) × 10³

Figure 3. Simulation of the progression of infection in a patch of epithelial tissue of size 360 μm x 360 μm starting from a single infected cell for a representative simulation using the baseline parameters given in Table 1. A. Snapshots of spatial configuration *vs* time, showing progression of a simulated infection. Columns, left to right: 0 minutes (time of initial infection), 4000 minutes (67 hours, 2 ¾ days) after infection, 8000 minutes (133 hours, 5 ½ days), 12000 minutes (200 hours, 8 ⅓ days), 16000 minutes (267 hours, 11 days), and 20000 (333 hours, 14 days) minutes (333 hours, 14 days). **First row:** epithelial-cell layer composed of uninfected (blue), infected (green), virus-releasing (red) and dead epithelial cells (black). **Second row:** position of immune cells in the extracellular environment layer. **Third row:** concentration of extracellular virus field. **Fourth row:** concentration of extracellular cytokine field. **Fifth row:** concentration of extracellular oxidative agent field. Fields are shaded on a logarithmic scale: red corresponds to the chosen maximum value specified in the first panel and blue corresponds to six orders of magnitude lower than the maximum value; colors saturate for values outside this range. **B-D.** Simulation time series. **B.** Number of uninfected (orange), infected (green), virus-releasing (red) and dead (purple) epithelial cells *vs* time on a logarithmic scale (0 values are overlaid at a non-logarithmic tick for clarity). **C.** Total extracellular cytokine (magenta) and total extracellular virus (brown) *vs* time on a logarithmic scale. **D.** Value of the immune recruitment signal S (yellow) and number of immune cells (grey) *vs* time on a linear scale. Simulations use periodic boundary conditions in the plane of the epithelial sheet, and Neumann conditions [46] normal to the epithelial sheet.

The infected cell immediately starts releasing cytokines into the extracellular environment. After an incubation period (of approximately 150 minutes, 2 ½ hours), the first infected epithelial cell (green) transitions from infected to virus releasing (red), and starts releasing viruses into the extracellular environment. Initial release of extracellular virus causes additional epithelial cells to become infected. Release of cytokines leads to delayed addition of immune cells to the simulation domain (Figure 3D). By 4000 minutes (67 hours, 2 ¾ days), the number of infected cells increases 10-fold and the epithelial cells infected at the beginning of the simulation start dying as a result of virally-induced death while the infection spreads outward from the initial site. As the number of infected cells and their cytokine production increase, the number of immune cells also increases. By 8000 minutes (133 hours, 5 ½ days), the number of dead epithelial cells around the initial infection site increases sharply. Following this phase of rapid cell death, the number of infected, virus-releasing and dead epithelial cells continues to increase exponentially but at a slower rate. This transition results in the formation of an annular region of infected cells spreading radially outwards from the initial infection site (Figure 3A), analogous to the Fisher equation for deterministic front propagation [47]. Total extracellular virus and cytokine continue to increase exponentially. The increase in cytokine results in continued recruitment of additional immune cells. By 16000 minutes (267 hours, 11 days), the number of uninfected epithelial cells reaches zero and the number of infected and virus-releasing cells peaks. Despite the declining number of infected and virus-releasing epithelial cells, the delayed immune response continues to add immune cells to the tissue. After about 16000 minutes (267 hours, 11 days), the extracellular virus and the amount of cytokine decrease exponentially as the remaining virus-releasing epithelial cells die. By 20000 minutes (333 hours, 14 days), all epithelial cells die and many immune cells leave the tissue.

Classification of spatiotemporal infection dynamics

The rate at which infection propagates and the strength (speed and amplitude) of the immune response depend on multiple model parameters. Interplay between these rates leads to a wide spectrum of qualitatively-distinct spatiotemporal dynamics. The virus-receptor binding affinity k_{on} and the immune response delay coefficient β_{delay} are critical parameters affecting the rate of infection of epithelial cells and the strength of the immune response, respectively. Larger k_{on} corresponds to a higher rate of infection propagation (increasing k_{on} increases the rate of internalization of extracellular viral particles into epithelial cells, see Equation (3) in *Models and methods*). Larger β_{delay} corresponds to weaker immune response (decreasing β_{delay} increases the strength of immune-cell recruitment, see Equations (12)-(14) in *Models and methods*).

Varying these two parameters around the baseline simulation values yields six patterns of spatiotemporal infection dynamics, ranging from unopposed infection to clearance (Figure 4). We defined these classes based on the transient dynamics and the final state of the simulation at 20000 minutes (333 hours, 14 days). We terminated the simulations at 20000 minutes (333 hours, 14 days) because we assume that, in real tissues, additional adaptive immune responses at this time generally lead to rapid viral clearance. As a result, any epithelial cells uninfected at the end of the simulation would likely remain uninfected if we included these additional immune mechanisms. We define the six patterns (*classes*) of infection dynamics as follows:

No immune response: a limiting case (corresponding to *in vitro* and organoid culture experiments on viral infection, which lack immune cells) that serves as a reference simulation showing the spread of unopposed infection. When the cellular immune response is absent, an infection front travels across the epithelium until all epithelial cells have died due to intracellular virus (Figure 4A and Figure S1).

Widespread infection: when the immune response is weak (large β_{delay}) or the rate of infection propagation is large (large k_{on}), the immune cells kill enough infected epithelial cells to reduce both the concentration of extracellular virus and the propagation of the infection front. However, at the end of the simulation no uninfected epithelial cells survive (Figures 3 and 4B).

Slowed infection: for moderate immune response (moderate β_{delay}) and a moderate rate of infection propagation (moderate k_{on}), both uninfected and infected epithelial cells and some extracellular virus remain at the end of the simulation (Figure 4C). These cases are functionally distinct from widespread infection, since even a single remaining uninfected epithelial cell could initiate tissue regeneration. In most cases of slowed infection, the numbers of infected cells and the extracellular virus continue to increase. A special case of slowed infection occurs when oscillations in the amount of virus (Figure S2A).

Containment: for strong immune response (small β_{delay}) and low to moderate rate of infection propagation (moderate k_{on}), a few infected and virus-releasing cells are present for most of the simulation. However, the immune cells eventually kill all infected and virus-releasing epithelial cells. At the end of the simulation, no infected or virus releasing cells remain, while

uninfected cells survive and some extracellular virus remains in the extracellular environment (Figure 4D).

Recurrence: for strong immune response (small β_{delay}) and a fast infection propagation (large k_{on}), relatively few epithelial cells become infected early in the simulation. All infected and virus-releasing epithelial cells die. However, the remaining extracellular virus infects additional epithelial cells later on, restarting the spread of infection (Figure 4E).

Clearance: for strong immune response (small β_{delay}) and a slow infection propagation (small k_{on}), the number of infected and virus-releasing epithelial cells goes to zero without recurrence and the extracellular virus drops below a threshold (of 1/900 per cell in our analysis), rendering the frequency of recurrence negligible (Figure 4F). A special case of clearance (**Failure to infect**) occurs when the initially infected epithelial cells fail to infect any other epithelial cells (Figure S2B).

To quantitatively characterize simulation results, we measured the number of uninfected, infected, virus-releasing and dead epithelial cells, the total number of immune cells, the number of activated immune cells, the total amount of extracellular virus (integral over the virus field), the total diffusive cytokine (integral over cytokine field), the maximum total extracellular virus (over all simulation time) and the maximum total diffusive cytokine (over all simulation time). Figure 4 shows these quantitative metrics, together with a series of spatial configurations for all model components, corresponding to each pattern of infection dynamics.

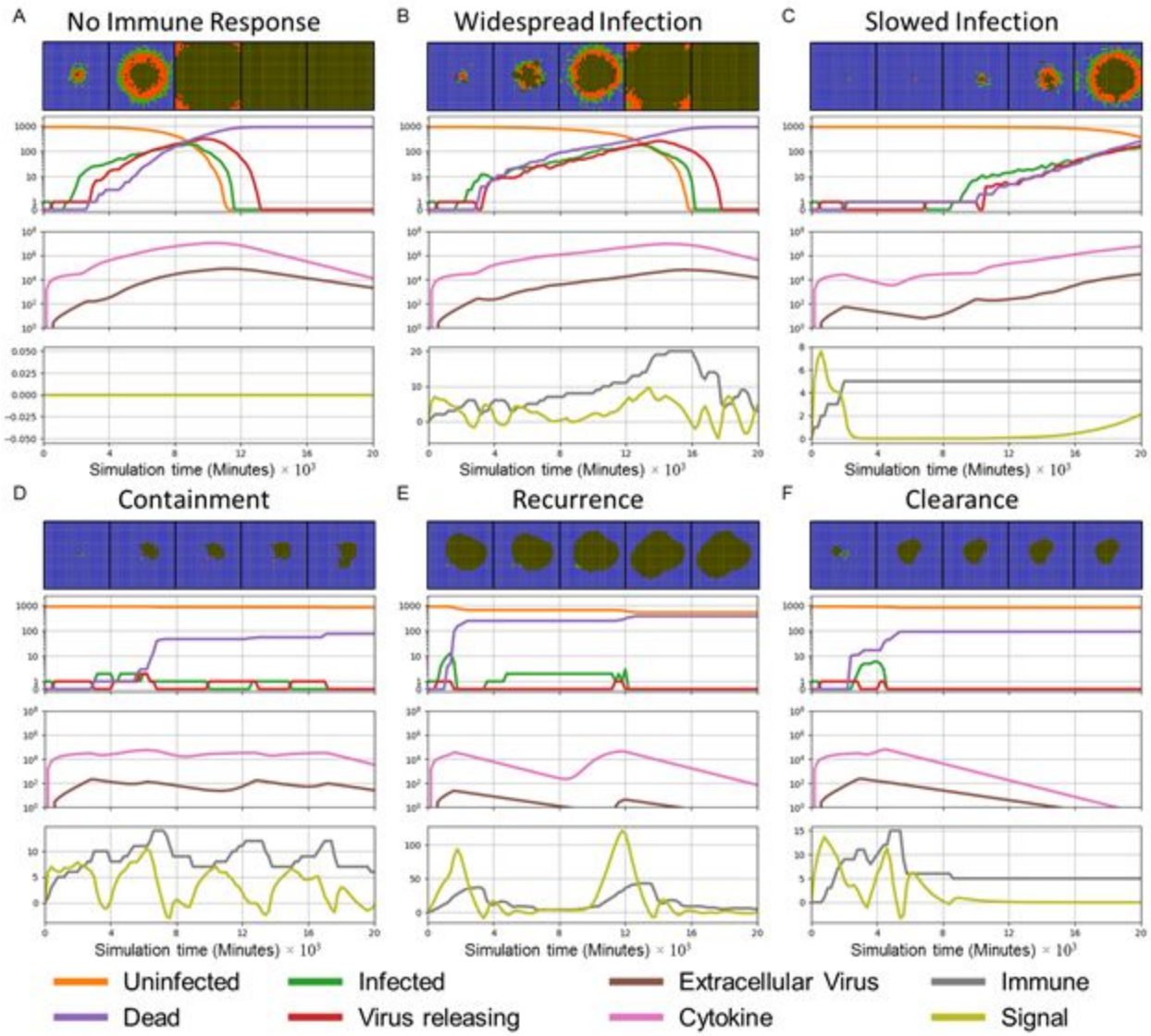

Figure 4. Patterns (classes) of spatiotemporal infection dynamics. First row: snapshots of spatial configurations of the epithelial cells. Color coded: uninfected (blue), infected (green), virus releasing (red), dead (black). TImes from left to right 4000 minutes (67 hours, 2 ¾ days), 8000 minutes (133 hours, 5 ½ days), 12000 minutes (200 hours, 8 ⅓ days), 16000 (267 hours, 11 days) and 20000 minutes (333 hours, 14 days). The right border of each snapshot aligns with the corresponding time in the time series. **Second row:** number of uninfected (orange), infected (green), virus-releasing (red) and dead (purple) epithelial cells *vs* time on a logarithmic scale (with 0 included for clarity). **Third row:** total extracellular cytokine (magenta) and total extracellular virus (brown) *vs* time on a logarithmic scale. **Fourth row:** value of the immune recruitment signal S (yellow) and number of immune cells (grey) *vs* time on a linear scale. **A. No immune response:** infection propagates unopposed until all epithelial cells have died from intracellular virus. **B. Widespread infection:** weak immune response slows propagation of the infection, but no uninfected cells survive at the end of the simulation. **C. Slowed infection:** uninfected and infected epithelial cells coexist at the end of the simulation. **E. Containment of infection:** no infected or virus-releasing epithelial cells remain, uninfected cells survive and virus remains in the extracellular environment at the end of the simulation. **F. Recurrence:** the number of infected and virus releasing epithelial cells goes to zero, but persistent extracellular virus infects new epithelial cells later on. **G. Clearance:** the number of infected and virus-releasing epithelial cells goes to zero and the level of

extracellular virus is negligible at the end of the simulation. The model in A. omits the immune response (components L1, I1-I4). All parameter values are as in Table 1 and Figure 3 except for k_{on} and β_{delay} (Table S1).

In the absence of an immune response, spread of the infection follows the diffusion of extracellular virus, resulting in concentric rings of different types of epithelial cells (see Figure 4A top row for epithelial cell types, Figure S1B shows the extracellular virus field). The viral propagation front, where uninfected epithelial cells transition to infected epithelial cells, moves radially outwards from the initial site of infection. Due to the stochastic internalization events, the front's outer contour is diffuse, with scattered infected epithelial cells ahead of the front, followed by a dense rim of infected and virus-releasing epithelial cells and a core of dead epithelial cells at the center. Similar waves, with a slower speed, are seen in the other cases where infection has occurred (Figure 4B and C top row).

Stronger immune response and lower rates of virus internalization promote containment of infection

To explore the effects of the rate of virus internalization and the strength of the immune response, we performed a multidimensional parameter sweep of the virus-receptor association affinity k_{on} and immune response delay coefficient β_{delay}. Variations in virus receptor association affinity represent factors that affect the binding affinity of cellular viral receptors (*e.g.*, ACE2 and TMPRSS-2 in the case of SARS-CoV-2) with a virus (*e.g.*, mutations in viral coat protein or drugs to block viral entry). Variations in immune response delay coefficient represent factors that affect the strength of the systemic immune response (*e.g.*, anti-inflammatory corticosteroids, IL-7 treatment or age, since older individuals tend to have slower adaptive immune responses)[36].

We ran ten simulation replicas for each parameter set, increasing and decreasing the baseline parameter values 10-fold and 100-fold (Figures 5-7). For each simulation replica, we examined the number of uninfected epithelial cells (Figure 5), the number of infected epithelial cells (Figure 6), the total extracellular virus (Figure 7), the number of dead epithelial cells (Figure S3), the number of virus-releasing cells (Figure S4) and the number of immune cells (Figure S5). We identified regions of the parameter space where all ten simulation replicas resulted in either containment/clearance (green-shaded subplots) or widespread infection (orange-shaded subplots). In the intermediate regions (unshaded subplots) different replicas for the same set of parameters exhibited other (and sometimes multiple) classes of dynamics.

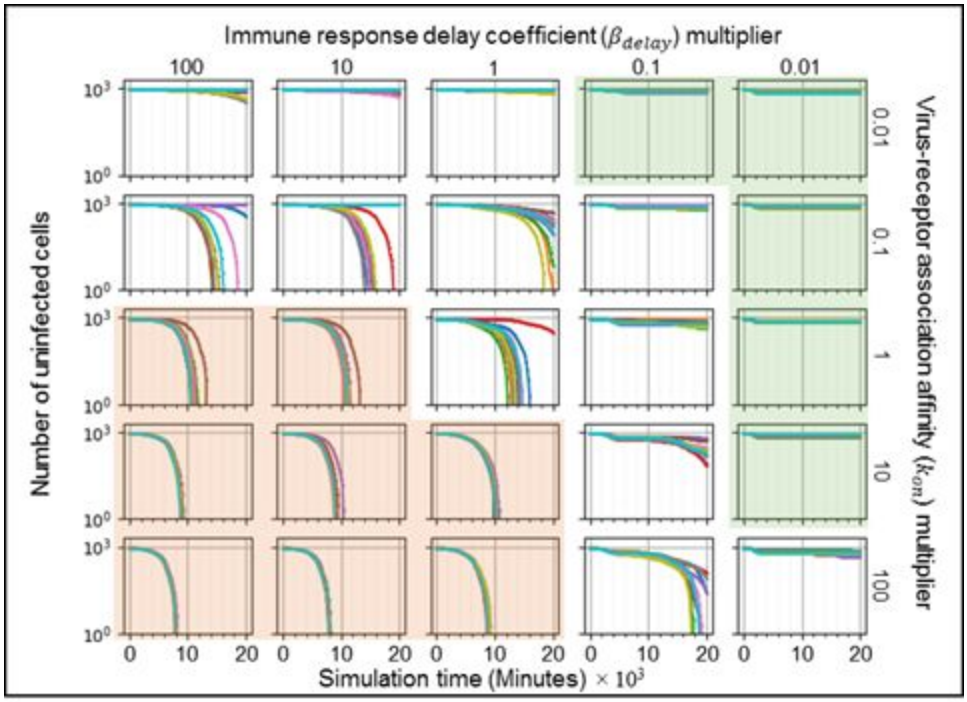

Figure 5. **Sensitivity analysis of the number of uninfected epithelial cells vs time for variations in virus-receptor association affinity k_{on} and immune response delay coefficient β_{delay}, showing regions with distinct infection dynamics**. Logarithmic pairwise parameter sweep of the virus-receptor association affinity k_{on} and the immune response delay β_{delay} ($\times 0.01$, $\times 0.1$, $\times 1$, $\times 10$, $\times 100$) around their baseline values, with ten simulation replicas per parameter set (all other parameters have their baseline values as given in Table 1). The number of uninfected epithelial cells for each simulation replica for each parameter set, plotted on a logarithmic scale, *vs* time displayed in minutes. See Figure 4 for the definitions of the classes of infection dynamics.

For large k_{on} and large β_{delay} (Figures 5-7, orange-shaded regions), all simulation replicas result in widespread infection and variability between simulation replicas is small. In this region, the initial release of virus into the extracellular environment results in a rapid increase in the number of infected and virus releasing epithelial cells early during the simulation, between 0 and 2000 minutes (0 to 33 hours, 0 to 1 ½ days) (Figure 6 and S4). Between 5000 and 20000 minutes (83 to 333 hours, 3 ½ to 14 days), the number of uninfected epithelial cells rapidly decays to zero. As in all simulation replicas with a large β_{delay}, the immune recruitment signal (Figure S6) is less responsive to the cytokine signal produced by infected and virus-releasing epithelial cells and no significant recruitment of immune cells occurs throughout the simulations (Figure S5). The number of virus-releasing epithelial cells peaks around 7500 minutes (125 hours, 5 days), the level of extracellular virus peaks around 9000 minutes (150 hours, 6 ¼ days) and the number of dead epithelial cells peaks around 10000 minutes (167 hours, 7 days, Figure S3). With no remaining uninfected epithelial cells to infect, all remaining infected epithelial cells become virus-releasing epithelial cells, which then die, causing the total amount of extracellular virus to decrease. .

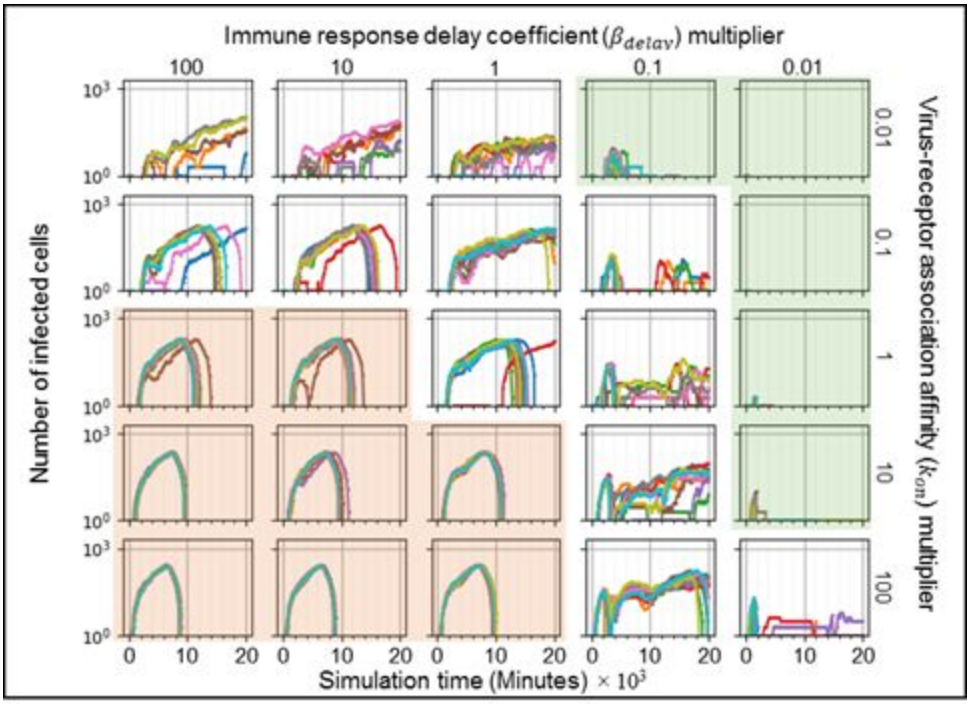

Figure 6. **Sensitivity analysis of the number of infected epithelial cells vs time for variations in virus-receptor association affinity k_{on} and immune response delay coefficient β_{delay}, showing regions with distinct infection dynamics**. Same parameter sweep as Figure 5. The number of infected epithelial cells for each simulation replica for each parameter set, plotted on a logarithmic scale, *vs* time displayed in minutes. See Figure 4 for the definitions of the classes of infection dynamics.

For small k_{on} and small β_{delay} (Figures 5-7, green-shaded subplots), all simulation replicas result in either clearance or containment and variability between simulation replicas is small. Initial release of virus to the extracellular environment results in a small change in the number of uninfected and infected epithelial cells. As in all simulation replicas with a small β_{delay}, the immune recruitment signal (Figure S6) is very sensitive to the cytokine produced by virus-releasing epithelial cells, resulting in rapid recruitment of immune cells and an early first peak in the population of immune cells around 2000 minutes (33 hours, 1 ⅓ days, Figure S5). In these simulations, the increase in the number of immune cells is followed by a rapid increase in the number of dead epithelial cells (Figure S3). The number of immune cells and the number of dead epithelial cells peak around the same time (2000 minutes, 33 hours, 1 ⅓ days), after which the number of immune cells decreases. With no remaining virus-releasing epithelial cells, the total extracellular virus decays until the infection is cleared. Increasing β_{delay} primarily increases the time when all infected epithelial cells have died.

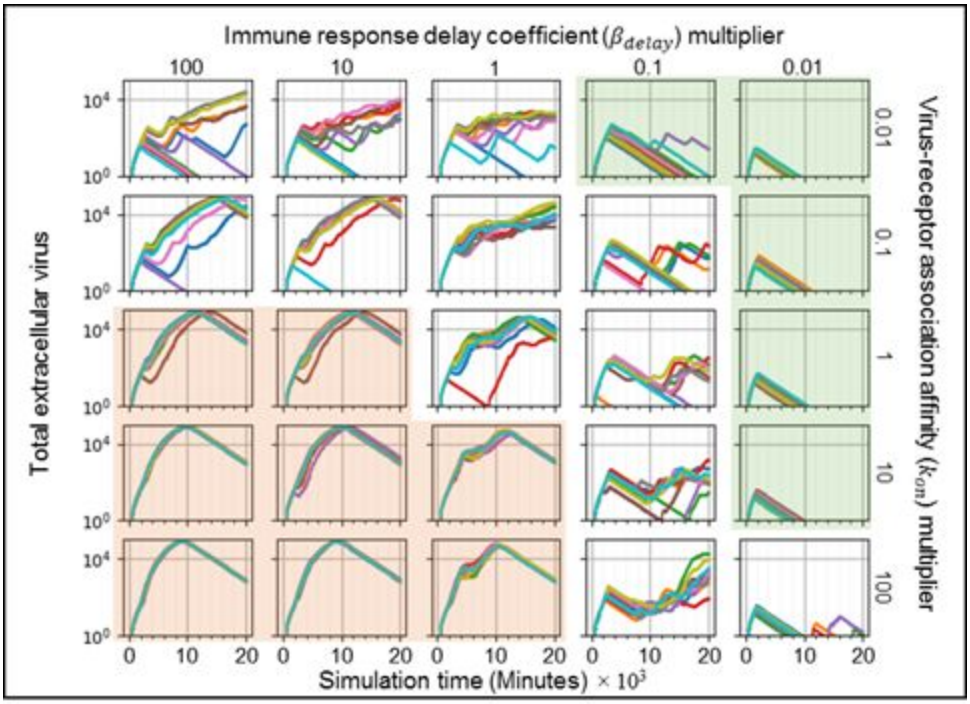

Figure 7. **Sensitivity analysis of the total amount of extracellular virus vs time for variations in virus-receptor association affinity k_{on} and immune response delay coefficient β_{delay}, showing regions with distinct infection dynamics**. Same parameter sweep as Figure 5. The total amount of extracellular virus for each simulation replica for each parameter set, plotted on a logarithmic scale, *vs* time displayed in minutes. See Figure 4 for the definitions of the classes of infection dynamics.

For moderate to high k_{on} and moderate to low β_{delay} (right unshaded subplots in Figures 5-7), the rate of new infection nearly balances the rate of elimination of infected and virus-releasing epithelial cells, resulting in replicas showing clearance, contaminant, recurrence and slowed infection for the same parameter values, with very few cases of widespread infection. The initial release of virus into the extracellular environment by the first virus-releasing epithelial cell infects a moderate number of uninfected epithelial cells. The resulting cytokine secretion elicits a moderate to high response of the immune recruitment signal (Figure S6) and number of immune cells (Figure S5). The early recruitment of immune cells leads to many epithelial cells dying before 4000 minutes (66 hours, 2 ⅔ days) (Figure S3). For a high probability of virus internalization (high k_{on}), even low amounts of extracellular virus are sufficient to cause recurrence. For moderate to low k_{on} and moderate to high β_{delay} (upper left unshaded subplots in Figures 5-7), rate of new infection of epithelial cells is slightly faster than the immune system's response, resulting in a combination of widespread infection, slowed infection and containment, and a few cases of clearance. The immune system is only moderately responsive to the cytokine signal, resulting in a slow to moderate increase in the immune recruitment signal (Figure S6) and in the number of immune cells (Figure S5). Cases of clearance and containment occur for a smaller final number of dead epithelial cells (Figure S3) compared to previously discussed cases.

Even moderate inhibition of genomic replication by antiviral therapies significantly reduces the spread of infection, but only when initiated soon after infection

Optimal therapeutic use of antiviral drugs requires considering the relationship between molecular *efficacy* (how effectively the drug blocks a particular aspect of the viral life cycle at saturation concentration), *potency of therapy* (the effect of the drug at a molecular level at a given dose) and clinical *effectiveness* (how well the drug reduces the severity or duration of the infection), as well as the tradeoff between side effects and bioavailability. One drug might have moderate efficacy but have few side effects. Another drug might have high efficacy, but have severe side effects at high doses that limit the maximum tolerated dose or use of even moderate doses in prophylaxis. A drug might also have a combination of beneficial and adverse effects (*e.g.*, it might reduce viral replication early in infection, but also be immunosuppressive) [13,37]. Antiviral drugs like Tamiflu retain their ability to block aspects of the viral life cycle (efficacy), but become much less clinically effective as the time before treatment increases: (in adults Tamiflu is most effective when given within 48 hours after exposure and thus is often used prophylactically) [38].

In this section we use our model to show the trade-offs between time-of-use and potency of a drug that targets viral genome replication in a host cell. Several antiviral medications for RNA viruses reduce the net viral replication rate by inhibiting synthesis of viral RNA by the viral RNA polymerase. We focus on RNA-synthesis blockers in this paper because viral genome synthesis exponentially increases the production rate of viruses per cell, while the other stages of viral replication have linear amplification effects (see Equations (6)-(9) in *Models and methods*).

To simulate the effects of treatment that targets RNA synthesis using different drug efficacies and times of administration, we generated a series of simulations in which we reduced r_{max}, the replication rate of genomic material in the viral replication model (Equation (7) in *Models and methods*), by different amounts and at different times in the simulation. The "viral replication multiplier" represents the potency of the treatment, the factor by which r_{max} is reduced (either a low dose with high efficacy, or a high dose with a less efficacy). The "time delay of application" is the simulation time at which r_{max} is reduced, which corresponds to the time after infection at which the treatment is administered. To characterize therapeutic effectiveness, we distinguished three classes of simulation outcomes:

Positive outcomes: effective treatment, where at least 50% of the epithelial cells remain uninfected at the end of the simulation (green-shaded subplots).

Negative outcomes: ineffective treatment, where less than 10% of the epithelial cells remain uninfected at the end of the simulation (orange-shaded subplots).

Intermediate outcomes: partially effective treatment, where between 50% and 10% of the epithelial cells remain uninfected at the end of the simulation (unshaded or intermediate-shaded subplots).

To characterize how the potency and time of initiation of treatment affect the dynamics of the simulation and treatment effectiveness, we examined the time courses of the number of uninfected epithelial cells (Figure 8), virus-releasing epithelial cells (Figure 9), the total amount of extracellular virus (Figure 10), the number of dead epithelial cells (Figure S7) and the number of immune cells (Figure S9). Intensity of green indicates the percent of simulation replicas that produced positive outcomes for a given set of parameters. Intensity of orange indicates the percent of simulation replicas that produced negative outcomes.

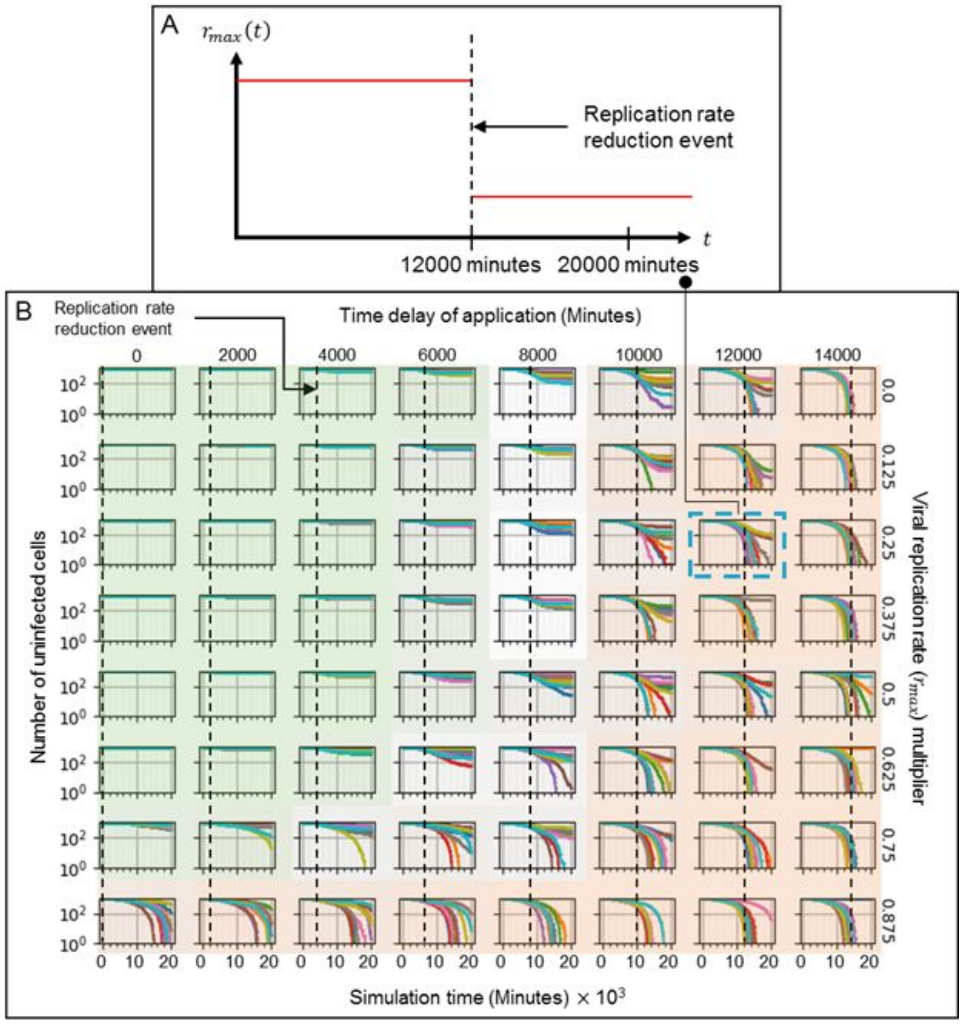

Figure 8. Number of uninfected cells vs time in simulations of a hypothetical drug treatment reducing the viral genome (*e.g.* RNA for SARS-CoV-2) replication rate (r_{max}) as a function of treatment potency and time of initiation of treatment. Drug therapy is administered at a fixed time after infection and remains activated for the duration of the simulation. **A**. Sample treatment, showing the time course of r_{max}. r_{max} is reduced by a multiplier which is one minus the potency of the drug at the given dose, 75% in **A**, at a particular time of initiation of treatment (time delay of application), 12000 minutes (200 hours, 8 ⅓ days) in **A**. **B**. A parameter sweep of the potency of

treatment (reduction in baseline viral replication rate r_{max}, vertical) and the time of treatment (dashed lines, horizontal) shows parameter regions where the majority of simulation replicas produce positive outcomes (green-shaded subplots), negative outcomes (orange-shaded subplots) and intermediate cases (intermediate shading or unshaded). Intensity of green and orange indicates the number of positive and negative outcome replicas for each parameter combination (treatment effectiveness). Green regions show that early intervention leads to positive outcomes (is effective) for most ranges of treatment potency, with high numbers of uninfected epithelial cells at the end of the simulation for almost all simulation replicas. Orange regions show that late interventions result in mostly negative outcomes (ineffective treatment) regardless of the potency, and that outcomes are more variable between replicas, with both positive and negative outcomes for most parameter sets. The number of uninfected epithelial cells for each simulation replica for each parameter set, plotted on a logarithmic scale, *vs* time displayed in minutes.

When the treatment is given early, while the level of extracellular virus is increasing rapidly and exponentially (before 6000 minutes, 100 hours, 4 days) after infection, most of the simulation replica outcomes are positive, showing effective treatment (Figures 9-11, green-shaded subplots). If the drug is administered prophylactically or very soon after infection (at 0 minutes) the treatment potency needs to be only 25% to achieve mostly positive outcomes (effective treatment). Increasing the time to treatment increases the potency required to achieve similar numbers of positive outcomes: the treatment is effective for a potency of at least 37.5% if administered by 4000 minutes (67 hours, 2 ¾ days), and at least 87.5% if administered by 6000 minutes (100 hours, 4 days). For all potencies greater than 12.5%, early intervention prevents significant increase in the number of virus-releasing cells (Figure 9, green-shaded subplots), and a small number of immune cells suffices to stop the spread of infection (Figure S9, green-shaded subplots). In this region, delaying treatment results both in a higher level of extracellular virus (Figure 10, green-shaded subplots) and more dead epithelial cells at the end of simulation (Figure 8, green-shaded subplots). With inhibited viral replication in the infected epithelial cells, the extracellular virus decays until it is mostly cleared by the end of simulation (Figure 10). Variability between simulation replicas for a given parameter set increases with both decreasing potency and increasing time of initiation of treatment.

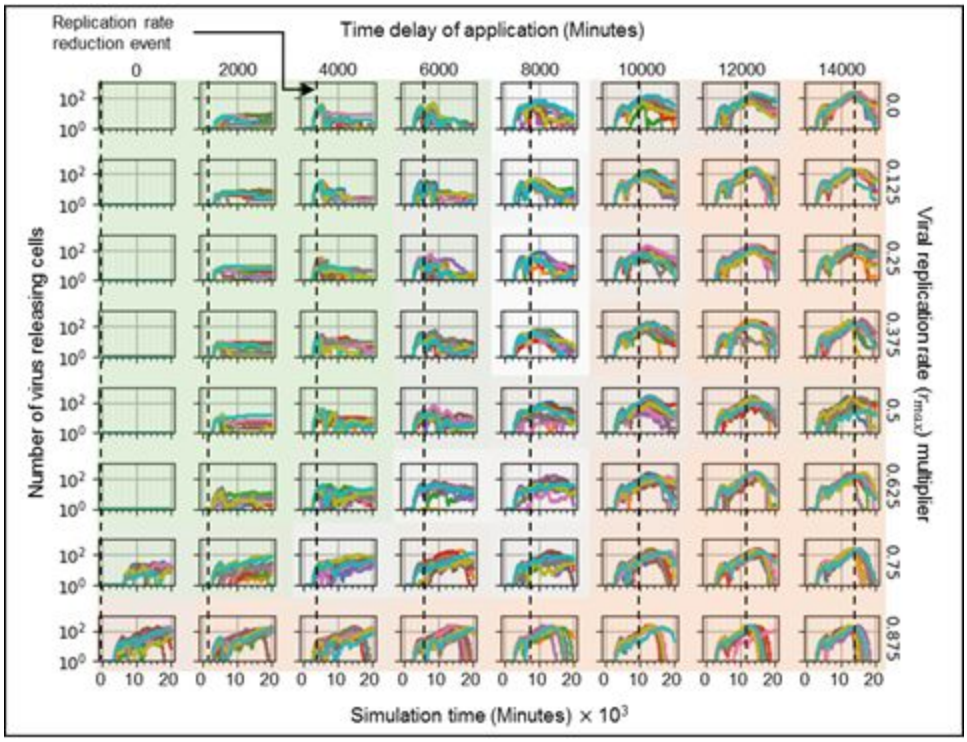

Figure 9. Number of virus releasing cells vs time in simulations of a hypothetical drug treatment reducing the viral genome (*e.g.* RNA for SARS-CoV-2) replication rate (r_{max}) as a function of treatment potency (one minus the viral replication rate multiplier) and time of initiation of treatment. The number of virus-releasing epithelial cells stays low when the intervention occurs early during infection (when the amount of extracellular virus is increasing rapidly), but continues to increase when the intervention occurs later (when the level of extracellular virus is at or near its maximum in the untreated case). Parameter values, axis types and time-scale and shading as in Figure 8.

If the potency of the treatment is 12.5% (or less), most of the simulation replicas have negative outcomes (low effectiveness), even if the drug is administered prophylactically or soon after infection (at 0 minutes) (Figures 9-11, bottom row). In these cases, the time after infection at which the drug is given makes no significant difference to the treatment effectiveness. When the treatment is given late (time delay of application of at least 10000 minutes, 167 hours, 7 days), regardless of the potency of the drug, most simulation replicas have negative outcomes (Figures 9-11, orange-shaded regions). By the time of treatment, a significant number of epithelial cells have been infected (more than 10% in most cases − Figure 9, orange-shaded regions) and a significant amount of virus has been released into the extracellular environment (Figure 10, orange-shaded regions). In addition, a significant number of epithelial cells have died (more than 10% in most cases − Figure S7, orange-shaded regions) and significant recruitment of immune cells has occurred (Figure S9, orange-shaded regions). For higher treatment potency, the level of virus in the extracellular environment starts decreasing immediately after treatment, even when a significant number of virus-releasing epithelial cells remain, indicating that viral replication inside cells has been significantly reduced. Later intervention also increases variability between simulation replicas and, although most simulation replicas have negative outcomes, the same set of parameter values produced two distinct

qualitative outcomes (some more and some less favorable) for higher potency (Figure S11, orange-shaded regions). Thus in a few cases, even late treatment can be effective.

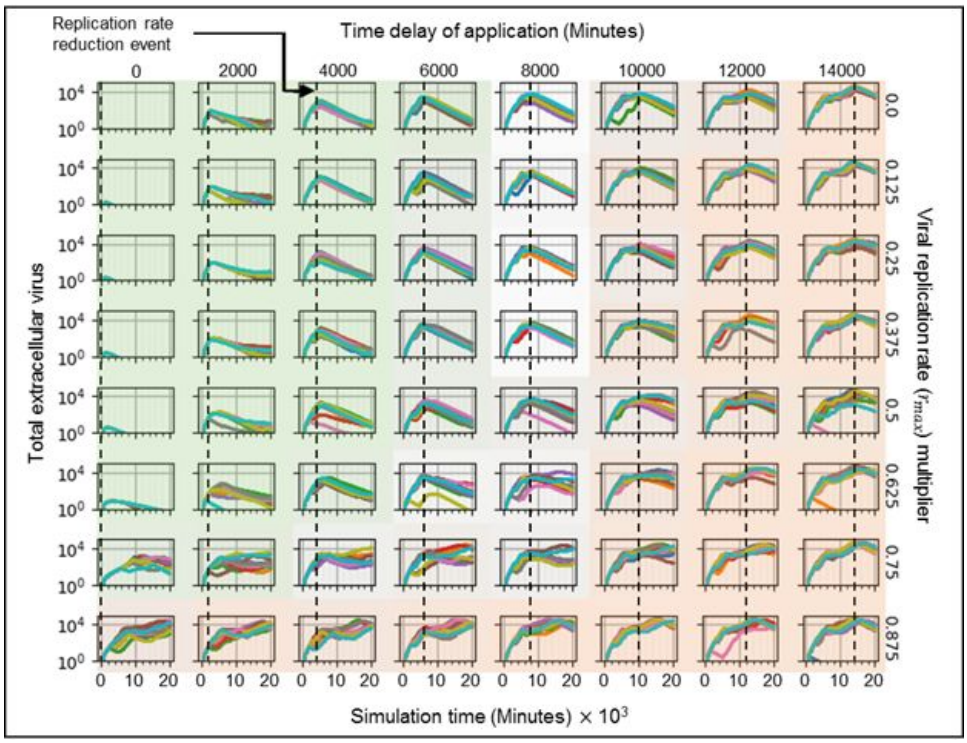

Figure 10. Levels of extracellular virus vs time in simulations of a hypothetical drug treatment reducing the viral genome (*e.g.* RNA for SARS-CoV-2) replication rate (r_{max}) as a function of drug potency (one minus the viral replication rate multiplier) and time of initiation of treatment. Extracellular virus is cleared or near-cleared when intervention occurs soon after infection. Parameter values, axis types and time-scale and shading as in Figure 8.

When the treatment is given at intermediate times (times between 6000 and 10000 minutes, 100 to 167 hours, 4 to 7 days), most simulation replicas have intermediate outcomes. For potencies above 50%, the fraction of uninfected epithelial cells at the end of simulation is relatively high (around 50%) and the treatment is usually moderately effective (Figure 8). For potencies below 50%, the number of virus-releasing epithelial cells remains approximately constant or continues to increase after treatment (Figure 9) and significant levels of extracellular virus remain at the end of the simulation, and so in most cases the treatment is ineffective (Figure 10). In this regime, variability between outcomes for the same parameter values is higher than for potencies above 50%.

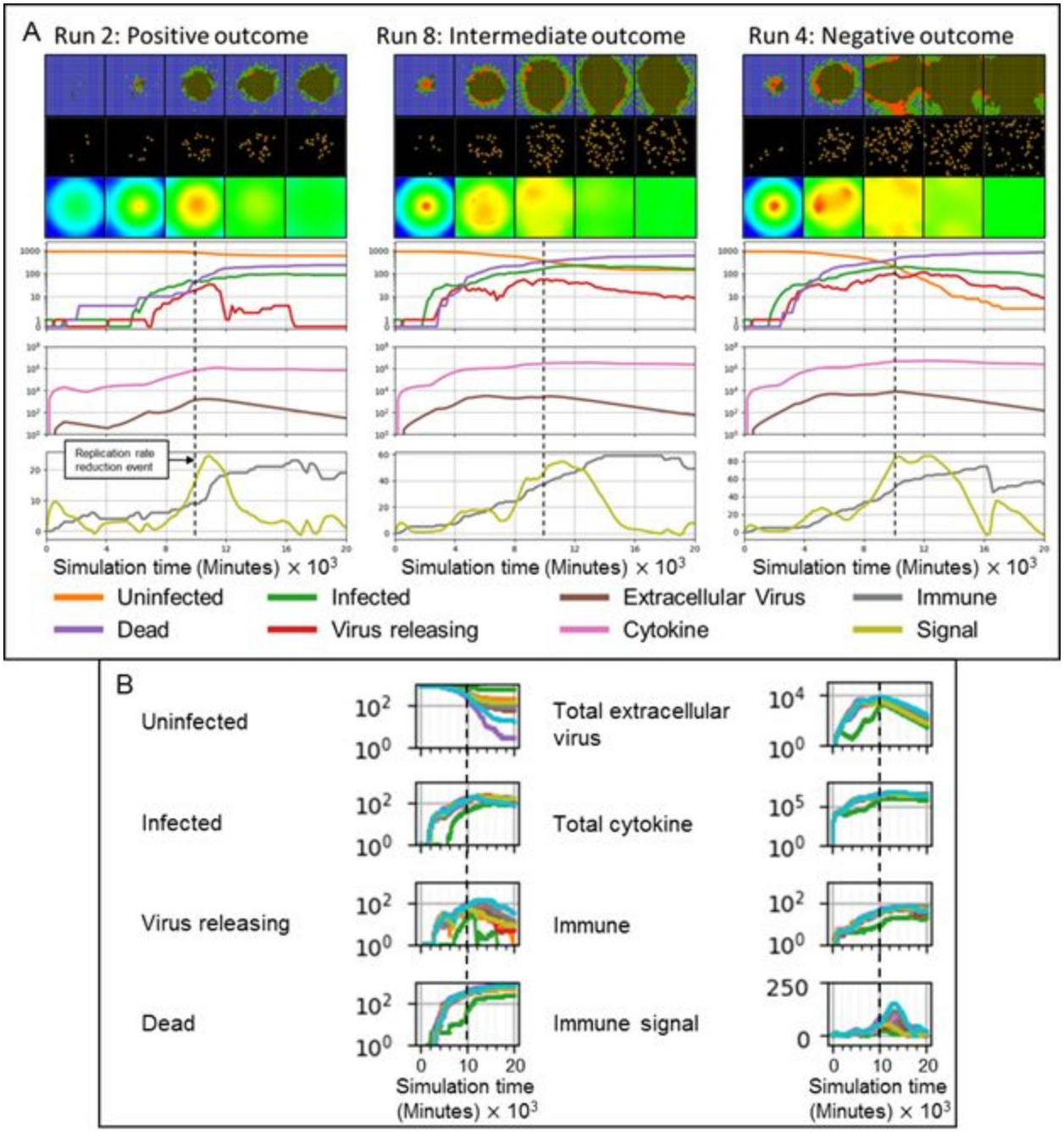

Figure 11. Difference in treatment effectiveness for different simulation replicas for perfect treatment potency (0 viral replication rate multiplier) near the time when the extracellular virus amount would reach its maximum in the untreated case (10000 minutes, 167 hours, 7 days). A. Select simulation replicas for this parameter set showing the variety of possible outcomes (treatment effectiveness). Spatial results show the epithelial and immune cell layers, and the extracellular virus field, at 4000, 8000, 12000, 16000, and 20000 minutes (67, 133, 200, 267 and 333 hours, 2 ¾, 5 ½, 8 ⅓ , 11 and 14 days). Cell type colors are the same as in Figure 3A. Virus field values are scaled as in Figure 3A. **B**. Time series for all simulation replicas for the selected parameter set: Right column, from top to bottom, number of uninfected epithelial cells, number of infected epithelial cells, number of virus-releasing epithelial cells, number of dead cells. Left column, from top to bottom: total amount of extracellular virus, total amount of cytokine, number of immune cells and immune response state variable. All variables except the immune signal plotted on a logarithmic scale *vs* time.

A particular parameter set (time delay of application of 10000 minutes, 100% potency) produced simulation replicas that had instances of all three outcomes (Figure 11). In a simulation replica with a positive outcome (Run 2, Figure 11A), the first uninfected epithelial cell dies (as well as a few uninfected epithelial cells) before 4000 minutes (67 hours, 2 ¾ days), after which the total extracellular virus gradually decreases. At around 4000 minutes (67 hours, 2 ¾ days), an epithelial cell near the initially-infected cell becomes infected, causing a recurrence of infection, whose spread was stopped by the treatment. In contrast, simulation replicas with intermediate and negative outcomes (Runs 8 and 4, respectively, Figure 11A) have comparable, and significantly more, numbers of infected and virus-releasing epithelial cells at 4000 minutes (67 hours, 2 ¾ days), while total extracellular virus is greater in the replicas with a negative outcome than in the replicas with an intermediate outcome. For the positive outcome replica, after 10000 minutes (167 hours, 7 days), the remaining extracellular virus infects just a few individual epithelial cells throughout the tissue. For the intermediate outcome replica, after 10000 minutes (167 hours, 7 days) the number of infected epithelial cells continues to increase until around 12000 minutes (200 hours, 8 ⅓ days) and then declines, while the number of uninfected epithelial cells slightly decreases at the end of the simulation. For the negative outcome replica, after 10000 minutes (167 hours, 7 days) the already depleted number of uninfected epithelial cells continues to rapidly decrease to near zero.

Discussion

Our spatial, multicellular model of primary acute viral infection of an epithelial tissue includes key aspects of viral infection, viral replication and immune response. By investigating sensitivity to model parameters and simulating drug therapies, we identified six distinct spatiotemporal classes of infection dynamics based on the model's transient behaviors and final configurations. Each of our simulation-defined classes corresponds to biologically or clinically observable factors and outcomes. The case of no immune response would be useful for analyzing *in vitro* experiments (*e.g.*, organoids). Widespread infection corresponds to an initial infection that is likely to spread to surrounding tissue and cause major tissue damage. Slowed infection corresponds to an initial infection whose spread is more likely to be eliminated by the adaptive immune response. Containment corresponds to immune-cell elimination of all infected cells but where remaining extracellular virus could result in new sites of infection elsewhere. Recurrence corresponds to the situation when new lesions form within the observed tissue patch. Clearance corresponds to immune-cell-based elimination of all infected cells and extracellular virus (classical viral clearance).

We showed that key parameters of the model, such as those affecting viral internalization (*i.e.*, virus-receptor association affinity k_{on}), can lead to both containment/clearance (*e.g.*, small k_{on}, Figures 5-7) and widespread infection (*e.g.*, large k_{on}, Figures 5-7). Multidimensional parameter sweeps showed how the interplay between immune

response (*e.g.* immune response delay coefficient β_{delay}) and viral spread could lead to widespread infection (*e.g.*, large β_{delay}, large k_{on}, Figures 5-7), rapidly cleared infection (*e.g.*, small β_{delay}, small k_{on}, Figures 5-7) or containment/clearance after substantial damage (*e.g.*, small β_{delay}, moderate k_{on}, Figures 5-7). Some of these outcomes would be expected biologically (*e.g.*, very fast internalization with a slow immune response is likely to lead to widespread infection; faster and stronger immune responses should control the spread of viral infection within the tissue [Figures 5-7]) and would also occur in deterministic non-spatial models. Others, like the coexistence of replicas with containment/clearance or failure to control for the same parameter set, are less expected, and could not occur in a deterministic non-spatial model (though they might occur in some stochastic non-spatial models).

We studied the influence of timing and potency of an RNA-polymerization inhibitor like remdesivir [48] on the spread of viral infection within tissue (Figures 9-11). As expected, in our model, drugs with this mode of action can improve viral control in tissue if administered prophylactically at high potency, and their effectiveness decreases the later they are administered. Less obviously, the lower-left region of Figures 9-11 shows how therapies with even reduced potency could control the infection when administered sufficiently early. While we expect prophylactic or early treatment at the same potency to be more effective than later treatment, our model suggests that, for antivirals, time of treatment is a more significant factor than potency in determining the effectiveness of the therapy. Our model thus suggests that drugs that interfere with virus replication are significantly more effective if used even at very low doses prophylactically or very soon after infection, than they would be if used even at a high dose as a treatment given later after exposure. Specifically, a prophylactic treatment in simulation which reduces the rate of viral RNA synthesis by only 35% (35% potency) is more effective than a treatment with 100% potency given two and a half days after infection, and has about the same efficacy as a treatment with 50% potency given one day after infection. Our model also showed that because of stochasticity in viral spread, later treatment at moderate to high potency may still be effective in a subset of individuals.

Both parameter sweeps had regions with little variation in outcome between replicas (*e.g.*, the upper-right and lower-left corners of Figure 5). In regions of the parameter space between these extremes (*e.g.*, the unshaded areas in Figures 5 and 9), different replicas showed dramatically different outcomes. One such parameter set in our drug therapy simulations produced three distinct qualitative outcomes (*i.e.*, positive, intermediate and negative outcomes, Figure 11). For these parameters, replica outcomes were particularly sensitive to stochasticity early in infection when only a few cells were infected (Figure 11A), with delayed spread of infection from the first infected cell producing more positive outcomes. Simulation replicas with negative outcomes (Figure 11A, Run 8) had higher extracellular virus levels at earlier times than those with intermediate outcomes (Figure 11A, Run 4), even though the fraction of each cell type was similar. Since the viral replication module is deterministic, the primary cause of this difference is the spatial distribution of cells. Spatial structure (*e.g.*, infection of neighboring cells), stochastic events (*e.g.*, early cell death of infected cells before significant

virus release) and cell-to-cell variation (*e.g.*, difference in viral release between cells) all affect the variation between replicas.

Differences in spatiotemporal dynamics and variability of outcomes thus critically depend on the ability of the model to resolve the spread of virus and immune response spatially. The intrinsic stochasticity of many model processes makes the spatial patterns of the infection front and distribution of tissue damage nontrivial. The spectrum of outcomes in our parameter sweeps (Figures 5-7 and 9-11) depends not only on parameter values and model immune response, but also on the emergent spatial patterns of cytokine and virus fields (*e.g.*, variations within the infection front expose different numbers of uninfected epithelial cells to the immune response).

Future perspectives

We can improve our model by including additional cellular and immune mechanisms discussed in Figure 1. Modules accounting for viral clearance, tissue recovery and persistent adaptive immune response can be added to model later stages of disease progression. The current immune model does not include important signaling factors (*e.g.*, interferon-induced viral resistance in epithelial cells) and the different roles of tissue-local and systemic signals (*e.g.*, various cytokines). It also omits many cell types associated with both innate and adaptive immune response and their roles (*e.g.*, viral scavenging by macrophages, relaying and amplification of immune signals by dendritic cells). The model does not currently consider the production and role of antibodies in the humoral immune response or tissue recovery after damage. The model also greatly simplifies the structure of the epithelium and its environment.

Our current results suggest priorities for improving the biological realism within existing modules, and for including modules representing additional biological components and mechanisms. We are currently implementing virus-scavenging by immune cells and local antiviral resistance due to Type 1-IFN paracrine signalling by epithelial cells. We are calibrating the virus replication module to existing experimental data for SARS-CoV-2 and influenza A. Because different tissues within the body have different responses to local viral infection, developing our framework to support the modeling and simulation of multi-organ disease progression (*e.g.*, by identifying model parameters corresponding to specific tissues and physiological compartments) would allow us to understand the highly variable whole-body progression of many viral diseases.

The immune response to viral infection depends on locus of infection, degree of infection and patient immune state. Understanding the reasons for immune failure to contain infection, or pathological responses like cytokine storms or sepsis, requires models of immune response at multiple locations and scales. The same is true for understanding and predicting the possible protective or adverse effects of coinfection. The number of permutations of infection timing and combination of pathogens is too large to address purely by experiments, but could be

addressed by simulations. Spatial modeling is also important because the spatiotemporal dynamics of coinfection within tissues may be important to the outcome (*e.g.*, whether individual cells can be superinfected, whether viral lesions with a tissue are disjoint or overlap, whether the main foci of the pathogens are in the same or different tissues).

We can also study the systemic effects of possible therapies with known molecular modes of action (as seen in *Results*). Evaluating therapies in a simulated context prior to performing animal or human trials could lead to more effective and rapid drug discovery and to optimized dosage and timing of treatments. Understanding the origins of population variability in disease progression is crucial to providing optimal personalized treatment. While the simulations presented here begin with a single infected cell, a simulation which begins with multiple infected cells might better represent the infection dynamics of patients that have been subject to high level exposure, such as healthcare workers. Factors such as hypertension, immunosuppression and diabetes affect tissue state and immune response and could also be incorporated into our model. More detailed studies of these factors using our model could reveal more about the effects of population variability (due to age, genetic variation, prior drug treatment or immune status) on disease progression.

We are working to implement validated non-spatial models of viral infection and immune response as agent-based spatial models (*e.g.*, viral production, cytokine secretion, tissue damage). By starting with a validated model that uses ordinary differential equations and adding spatial components gradually, we can calibrate our spatial models and validate our results. We can also conduct simultaneous, cross-platform validation of spatial models by building multiple implementations of the same conceptual and quantitative models on independent modeling platforms (here Chaste [49,50] and Morpheus [51]).

The COVID-19 crisis has shown that drug discovery and therapy development both require new predictive capabilities that improve their effectiveness and efficiency. We have developed our framework to explore the relationship between molecular, cellular-level and systemic mechanisms and outcomes of acute viral infections like SARS-CoV-2, and to support development of optimal, patient-specific treatments to combat existing and new viruses.

Models and methods

First we present the model as a high-level conceptual model where we list each process included in an implementation-independent manner. We then detail the quantitative model and its computational implementation, which uses a Cellular Potts representation of cellular dynamics.

Conceptual model: biological hypotheses and assumptions

As discussed in *Introduction* (Figure 2A) we consider an epithelial tissue and a lymph node. The tissue contains two interacting spatial components: an epithelium component (consisting of a monolayer of epithelial cells), and an extracellular environment component (containing immune cells, extracellular virus and chemicals). The lymph node component (whose state is affected by signaling from the tissue) adds immune cells to the extracellular space when in a proinflammatory state and removes them when in an anti-inflammatory state. A set of processes and interactions govern how the states of these components evolve in time. We detail these components, processes and interactions in the following subsections and in Figure 2.

Epithelium component

The epithelium component represents the layer of epithelium in the tissue, and is composed of epithelial cells of four types (Figure 2C), uninfected, infected, virus-releasing and dead. We assume that the epithelial cells are immobile. The epithelial cells contain modules that describe the viral life cycle and approximate the amount of virus as a continuous quantity (Figure 2B), including: binding and internalization of viral particles from the extracellular environment (**E1**), intracellular replication (**E2**) and release (**E3**) of synthesized virus into the extracellular environment, as well as cell death caused by viral-replication-associated damage, immune-cell killing and oxidative agent killing (**E4**).

E1 - Viral internalization

Models extracellular virus binding to epithelial cell receptors and internalization (including endocytosis-dependent and -independent routes). Internalization of viral particles involves binding of the viral spike protein to target cell-surface receptors, truncation by surface proteins and receptor-mediated endocytosis or fusion with the host plasma membrane. We assume the dynamics of internalization can be represented by describing the dynamics of virus-surface-receptor binding, determined by the amount of extracellular virus and target surface receptors, and by the binding affinity between them (**T1**→**E1**). We also consider the dynamic depletion of unbound target surface receptors on a cell when it internalizes a virus and superinfection of infected cells. Internalized viral particles initiate the viral replication process (**E1**→**E2** and Figure 2B).

E2 - Viral replication

Models the viral replication cycle inside a host epithelial cell (Figure 2B). Individual cells infected with many non-lytic viruses show a characteristic three-phasic pattern in their rate of viral release. After infection and during an *eclipse phase*, a cell accumulates but does not yet release newly assembled viruses. In a second phase, the rate of viral release increases exponentially until the virus-releasing cell either dies or, in a third phase, saturates its rate of virus synthesis and release. Viral replication hijacks host synthesis pathways and may be limited by the availability of resources (amino acids, ATP, *etc.*), synthesis capability (ribosomes,

endoplasmic reticulum, *etc.*) or intracellular viral suppression. A quantitative model of viral replication needs to be constructed and parameterized such that it reproduces these three phases.

We model viral replication based on processes associated with positive sense single-stranded RNA (+ssRNA) viruses. +ssRNA viruses initiate replication after unpacking of the viral genetic material and proteins into the cytosol (**E1→E2)**. The viral RNA-dependent RNA polymerase transcribes a negative RNA strand from the positive RNA strand, which is used as a template to produce more RNA strands (denoted by "Viral Genome Replication" in Figure 2B). Replication of the viral genome is the only exponential amplification step in the growth of most viruses within cells. Subgenomic sequences are then translated to produce viral proteins ("Protein Synthesis" Figure 2B). Positive RNA strands and viral proteins are transported to the endoplasmic reticulum (ER) where they are packaged for release. After replication, newly synthesized viral genetic material is translated into new capsid protein and assembled into new viral particles ("Assembly and Packaging" in Figure 2B). These newly assembled viral particles initiate the viral release process (**E2→E3**). We assume the viral replication cycle can be modeled by defining four stages: unpacking, viral genome replication, protein synthesis, and assembly/packaging. Figure 2B illustrates these subprocesses of replication and their relation to viral internalization and release.

E3 - Viral release

Models intracellular transport of newly assembled virions and release into the extracellular environment (**E3→T1** and Figure 2B "Release"). We conceptualize the virus being released into the extracellular fluid above the apical surfaces of epithelial cells. Newly assembled virions are packed into vesicles and transported to the cell membrane for release into the extracellular environment (**E2→E3**). We assume that no regulation occurs after assembly of new virus particles, and that release into the extracellular environment can be modeled as a single-step process (**E3→T1**).

E4 - Cell death

Models death of epithelial cells due to various mechanisms. Models the combined effect of the many types of virus-induced cell death (*e.g.*, production of viral proteins interferes with the host cell's metabolic, regulatory and delivery pathways) as occurring due to a high number of assembled viral particles in the viral replication cycle (**E2→E4**). Models cell death due to contact cytotoxicity (**I3→E4**). Models cell death due to oxidizing cytotoxicity (**T3→E4**).

Extracellular environment component

The extracellular environment contains the immune cells, extracellular virus, cytokines and oxidative agent, and is the space where transport of viral particles (**T1**), cytokine molecules (**T2**) and the oxidizing agent (**T3**) occurs. Immune cells are mobile and can be either activated or inactive (**I1**). Inactive immune cells move through random cell motility and activated immune cells chemotax along the cytokine field (**I2**). The immune cell modules also account for cytotoxic

effects of immune cells on contact due to antigen recognition (**I3**) and through the secretion of oxidizing agents (**I4**).

T1 - Viral transport

Models diffusion of viral particles in the extracellular environment and their decay. Viral particles are transported by different mechanisms (*e.g.*, ciliated active transport, diffusion) and media (*e.g.*, air, mucus) at different physiological locations and through different types of tissue (*e.g.*, nasopharyngeal track, lung bronchi and alveoli). Viral particles are eliminated by a variety of biological mechanisms. We represent these mechanisms by modeling transport of viral particles as a diffusive virus field with decay in the extracellular environment. We model transport in a thin layer above the apical surfaces of epithelial cells. Viral internalization results in the transport of a finite amount of virus from the extracellular environment into a cell and depends on the amount of local extracellular virus and number of cell surface receptors (**T1-E1**). Infected cells release viral particles into the extracellular environment as a result of the viral replication cycle (**E3-T1**).

T2 - Cytokine transport

Models diffusion and clearance of immune signaling molecules in the extracellular environment. The immune response involves multiple signaling molecules acting upon different signaling pathways. We assume that the complexity of immune signaling can be functionally represented using a single chemical field that diffuses and decays in the extracellular environment. Once infected, epithelial cells secrete signaling molecules to alert the immune system (**E2-T2**). Locally, exposure to cytokine signaling results in activation of immune cells (**T2-I1**). Upon activation, immune cells migrate towards infection sites guided by cytokine (**T2-I2**). Lastly, activated immune cells amplify the immune signal by secreting additional cytokines into the extracellular environment (**I1-T2**). We model long-range effects by assuming that cytokine exfiltrates tissues and is transported to immune recruitment sites (**T2-L1**).

T3 - Oxidizing agent burst and transport

Models diffusion and clearance of a general oxidizing agent in the extracellular environment. One of the cytotoxic mechanisms of immune cells is the release of different oxidizing agents, reactive oxygen species (*ROS*) like H_2O_2 and nitric oxide (*NO*). The mechanism of action of such agents varies but we assume that we can generalize such effects by modeling a single diffusive and decaying oxidizing agent field in the extracellular environment. The oxidizing agent is secreted by activated immune cells after persistent exposure to cytokine signals (**I4→T3**). We assume that the range of action of the oxidizing agent is short. Cell death is induced in uninfected, infected and virus-releasing epithelial cells when sufficiently exposed to the oxidizing agent (**T3→E4**).

I1 - Immune cell activation:

Models immune cell maturation due to cytokine signaling. Immune cells mature at the recruitment site before being transported to the infection site as inactive immune cells

(**L1→Immune Cells**). After infiltration, immune cells need to be exposed to local cytokine signals before activating (**T2→I1**). Once activated, immune cells chemotax along the cytokine field (**I2**) and amplify immune signaling by releasing cytokine molecules into the extracellular environment (**I1→T2**). Immune cells can also deactivate after a period of activation (**I1** and Figure 2C).

I2 - Immune cell chemotaxis

Models activated immune cell chemotactic migration towards infection sites. We assume that upon activation (**I1→I2**), immune cells move preferentially towards higher concentrations of local cytokine (**T2→I2**).

I3 - Immune cell direct cytotoxicity and bystander effect

Models immune cell cytotoxicity when immune cells (both activated and inactive) identify and induce death in epithelial cells with internal virus. Immune cells identify epithelial cells with internal virus on contact by antigen recognition and induce cell death by activating the caspase cascade (**I3→E4**). Uninfected, infected, and virus-releasing epithelial cells in contact with an epithelial cell that is killed by direct cytotoxicity can die through a bystander effect.

I4 - Immune cell oxidizing agent cytotoxicity

Models activated immune cell killing of target cells through the release of a diffusive and decaying oxidizing agent into the environment. Cell death is induced in uninfected, infected and virus-releasing epithelial cells when sufficiently exposed to the oxidizing agent (**T3→E4**).

Lymph node component

The lymph node component models the net pro- or anti-inflammatory state of the immune system. It responds to cytokines received from the tissue and adds or removes immune cells from the tissue (**L1**).

L1 - Immune cell recruitment

Models immune cell recruitment and infiltration into the tissue in response to cytokine signaling by infected cells and activated immune cells. Infected cells secrete signaling molecules into the extracellular environment (**E2→T3**), which alerts resident immune cells and recruits new immune cells from the blood, distant lymph nodes and bone marrow. We model the local strength of the cytokine signal as causing an increase in the strength of the signal at the immune recruiting sites. We model long-distance signaling by assuming that cytokine molecules in the extracellular environment exfiltrate the infection site and are transported through the lymphatic system to the lymphatic system to lymph nodes and through the bloodstream to initiate immune-cell recruitment (**T2→L1**). A delay on the order of minutes to hours would represent semi-local recruitment (*e.g.*, at the blood vessels). A delay on the order of days would represent long-range, systemic recruitment (*e.g.*, the time required for a dendritic cell to reach a

lymph node and an induced T cell to return). Recruited immune cells are then transported and infiltrate the infection site (**L1→Immune Cell**).

Quantitative model and implementation

For model construction and integration we use the open-source multicellular modeling environment CompuCell3D (www.compucell3d.org) which allows rapid and compact specification of cells, diffusing fields and biochemical networks using Python and the Antimony language [45,52]. Compucell3D is specifically designed to separate model specification (conceptual and quantitative models) from the details of model implementation as a simulation and to make simulation specification accessible to biologists and others not specializing in software development. In this paper, we specifically designed the Python modules and their cross-scale integration to have clear and stable APIs, allowing modules to be rapidly swapped out by collaborating developers. CompuCell3D runs on Windows, Mac and Linux platforms without change of model specification, and allows cluster execution for parameter exploration.

Cellular Potts model (CPM)

Cell types

Cells are divided into two broad groups, epithelial and immune cells, and have a *type* (see Figure 2C) which determines their properties, the processes and interactions in which they participate, and their events and dynamics. Epithelial cells can have one of four types (uninfected, infected, virus releasing and dead). Immune cells can have one of two types (activated and inactive). Cell types can change according to outcomes of various modules, and a module specifying such an event describes both the initial and final cell types of the transition. A cell type in the model is not a phenotype in the biological sense (*e.g.*, *epithelial* cell), but an identifier for the various states that a particular cell can assume (*e.g.*, *dead epithelial* cell). When an epithelial cell changes to the dead type, all epithelial modules are disabled and the cell is generally inactive.

Cellular dynamics

Cellular spatial dynamics is modeled using the Cellular Potts model (also known as *CPM*, or Glazier-Graner-Hogeweg model), which represents generalized cells and medium as occupying a set of sites in a lattice [53]. Random cell motility is modeled as the stochastic exchange of sites at intercellular and cell-medium interfaces. Configurations evolve to minimize the system's effective energy $\mathcal{H}$,

$$\mathcal{H} = \sum_{\sigma} \lambda_{volume} (v(\sigma) - V(\tau(\sigma)))^2 + \sum_{x} \sum_{x' \in N(x)} \left(1 - \delta_{\sigma(x),\, \sigma(x')}\right) J(\tau(\sigma(x)),\ \tau(\sigma(x'))) + \mathcal{H}_{chemotaxis}. \quad (1)$$

Here σ is the integer identification of a cell and $\tau(\sigma)$ is the type of cell σ. $v(\sigma)$ and $V(\sigma)$ are the current and target volumes of cell σ, respectively, and λ_{volume} is a volume constraint coefficient. $N(x)$ is the neighborhood of site x, $\delta_{i,j}$ is the Kronecker-delta, and $J(\tau, \tau')$ is the effective contact energy per unit surface area between cells of types τ and τ'. The final term, $\mathcal{H}_{chemotaxis}$, models chemotaxis-directed cell motility, and is prescribed by module I2. The cell configuration evolves through asynchronous lattice-site copy attempts. A lattice-site copy attempt starts by random selection of a site x in the lattice as a target, and a site x' in its neighborhood as a source. A configuration update is then proposed in which the value x' from the source site overwrites the value of x in the target site. The change in total effective effective energy $\Delta\mathcal{H}$ due to the copy attempt is calculated, and the update is executed with a probability given by a Boltzmann acceptance function,

$$\Pr(\sigma(x) \rightarrow \sigma(x')) = e^{-\max\{0, \frac{\Delta\mathcal{H}}{\mathcal{H}^*}\}}. \tag{2}$$

Here the intrinsic random motility $\mathcal{H}^*$ controls the stochasticity of accepted copy attempts. Updates that reduce the system's effective energy are always accepted. The unit of simulation time is the Monte Carlo step (*MCS*)−taken to be 20 minutes in this work. One MCS corresponds to considering a number of copy attempts equal to the number of lattice sites.

Epithelial component modules

Processes **E1**-**E4** describe epithelial cell functions as defined below. **E1**, **E2** and **E4** govern the cell-type transitions of epithelial cells (see Figure 13). **E1** transforms an uninfected epithelial cell into an infected epithelial cell. **E2** transforms an infected epithelial cell into a virus-releasing epithelial cell. **E4** transforms a virus-releasing epithelial cell into a dead cell.

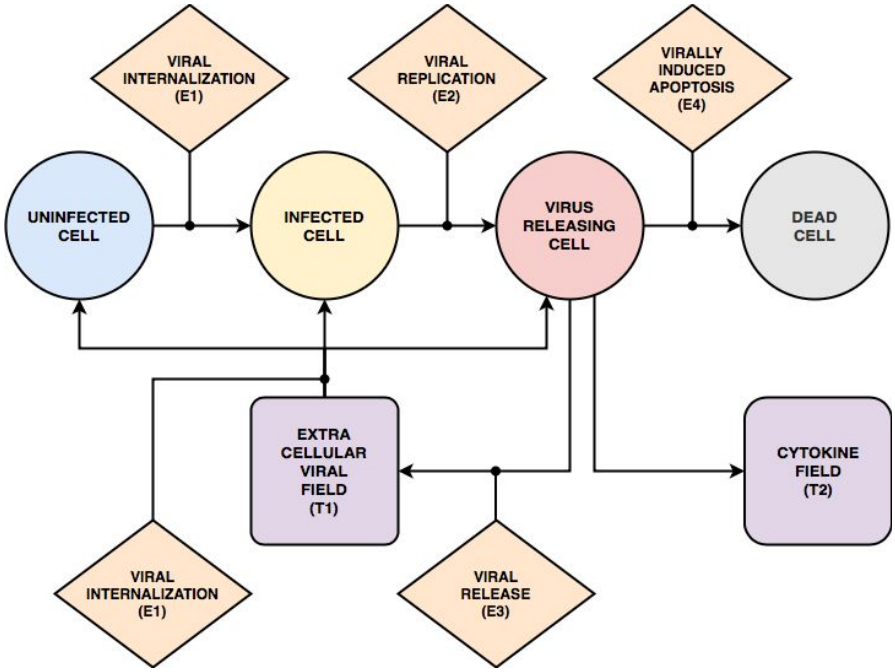

Figure 13. State diagram and interactions of epithelial cells. Epithelial cells can have one of four "cell types": uninfected, infected, virus-releasing and dead. Uninfected cells become infected cells when the viral uptake model (**E1**) internalizes viruses from the extracellular virus field (**T1**). Infected cells continue internalizing viruses from the extracellular virus field and become virus-releasing cells when the viral replication model (**E2**) produces sufficient newly assembled virions. Virus-releasing cells secrete viruses into the extracellular virus field (**T1**) according to the viral release module (**E3**) and secrete cytokines directly into the extracellular cytokine field (**T2**). Virus-releasing cells can die if the conditions of the virally induced cell-death model (**E4**) are met.

E1 - Viral internalization

To capture the stochasticity associated with internalization of discrete virus particles in terms of discrete binding events, we assign each uninfected, infected and virus-releasing epithelial cell a probability of absorbing diffusive viral particles from the extracellular virus field (**T1**). The uptake probability $\Pr(Uptake(\sigma) > 0)$ for each cell σ is given by a Hill equation of the total amount of diffusive viral particles in the domain of the cell $c_{vir}(\sigma)$, the number of unbound cell surface receptors $SR(\sigma)$ and the binding affinity between them.

$$\Pr(Uptake(\sigma) > 0) = \frac{\Delta t}{\alpha_{upt}} \frac{(c_{vir}(\sigma))^{h_{upt}}}{(c_{vir}(\sigma))^{h_{upt}} + V_{upt}{}^{h_{upt}}}, \text{ where } V_{upt} = \frac{R_o k_{off}}{2k_{on}\nu(\sigma)SR(\sigma)}. \quad (3)$$

Here h_{upt} is a Hill coefficient, R_o is the cell's initial number of unbound receptors, k_{on} is the virus-receptor association affinity, k_{off} is the virus-receptor dissociation affinity, α_{upt} is a characteristic time constant of uptake and Δt is the time represented by one MCS. At each simulation time step, the uptake probability is evaluated against a uniformly-distributed random variable. When uptake occurs, the uptake rate is proportional to the local amount in the virus

field (**T1**), and the probability of uptake is used to define the amount ($Uptake$) of virus taken up during the MCS,

$$Uptake(\sigma) = \frac{1}{\Delta t}\Pr(Uptake(\sigma) > 0)c_{vir}(\sigma), \tag{4}$$

$$\frac{dSR(\sigma)}{dt} = -Uptake(\sigma). \tag{5}$$

The amount absorbed by each cell ($Uptake$) is uniformly subtracted from the virus field over the cell's domain and the cell's number of cell surface receptors is reduced by the same amount. The amount of virus taken up ($Uptake$) is also passed to the cell's instance of the viral replication model (**E2**). Infected epithelial cells continue taking up viral particles from the environment until their cell surface receptors are depleted.

E2 - Viral replication

Our viral replication model combines equations and parameters from several sources to represent the replication of a generic virus [6,10,18,43]. The model contains four variables representing different states of the viral replication process: unpacking U (Equation (6)), viral genome replication R (Equation (7)), protein synthesis P (Equation (8)) and assembly and packaging of new virions A (or simply "assembled", Equation (9)). Biologically, the only process which can exponentially increase the rate of virus production by a single cell is viral genome replication, so the equations include the positive feedback by R in Equation (7). Biologically, factors like the cell's metabolism, limited number of ribosomes, maximum rate of endoplasmic reticulum function and activation of intracellular viral suppression pathways all limit production of viral components, so we include a Michaelis-type saturation term for the rate of replication in Equation (7). Each uninfected, infected and virus-releasing cell in the simulation contains an independent copy of the system of ordinary differential equations modeling the viral replication process,

$$\frac{dU}{dt} = Uptake - r_u U, \tag{6}$$

$$\frac{dR}{dt} = r_u U + r_{max} R \frac{r_{half}}{R + r_{half}} - r_t R, \tag{7}$$

$$\frac{dP}{dt} = r_t R - r_p P, \tag{8}$$

$$\frac{dA}{dt} = r_p P - Release. \tag{9}$$

Here r_u is the unpacking rate, r_{max} is the viral replication rate, r_t is the translating rate (rate at which viral genomes turn into RNA templates for protein production) and r_p is the packaging rate. $Uptake$ is defined in **E1** and $Release$ is defined in **E3**. The saturation of the rate of viral genome replication is represented by a Michaelis-Menten function, $\frac{r_{half}}{R + r_{half}}$, where r_{half} is the

amount of R at which the viral genome replication rate is reduced to $\frac{r_{max}}{2}$. The duration of the eclipse phase of single-cell infection (the time between the first entry of the virus into the cell and the first release of newly synthesized virus) is approximately $t_{eclipse} \approx \frac{1}{r_u} + \frac{1}{r_{max}} + \frac{1}{r_t} + \frac{1}{r_p}$ (11.7 hours for the reference parameter set in Table 1), with the additional complication that in our model, an epithelial cell does not release virus until A reaches a threshold value. The timescale for tenfold increase of virus release when viral replication is maximal is $t_{10} \approx \frac{log(10)}{r_{max}}$ (7.7 hours for the reference parameter set in Table 1). The number of newly assembled virions is passed to the cell's instance of the viral release module (**E3**). See Figure 2B for a schematic of the viral replication process and Figure 14 for a representative time series from the viral internalization, replication and release modules.

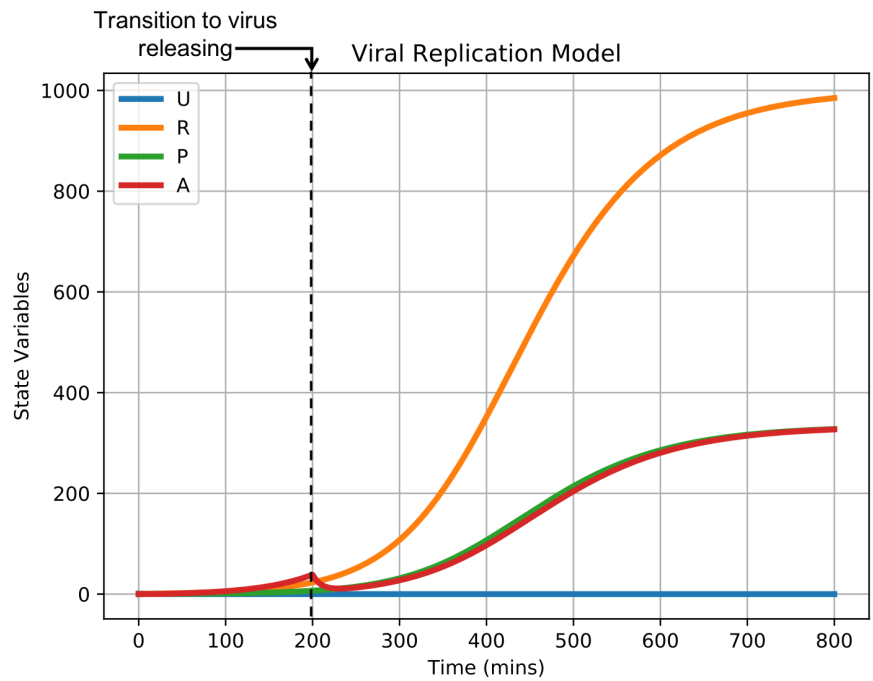

Figure 14. Representative time series of viral internalisation, replication and release models from Figure 2B. A sample simulation of the viral replication model in a single epithelial cell. The model is initialized with one unit of virus in the unpacking state (U = 1), and the rest of the state variables set to zero (R = 0, P = 0, A = 0). No additional virus internalization occurs during this sample simulation. Dashed line indicates the time of the cell's transition from the infected to virus-releasing cell type.

E3 - Viral release

Virus releasing cells release viral particles into the extracellular virus field (**T1**). The amount of virus released by a cell per unit time is proportional to the state variable for assembled virions in the viral replication module (**E2**),

$$Release = r_s A. \tag{10}$$

Here r_s is the release rate of viral particles and A is the level of assembled virus in the cell (defined in **E2**). The total amount released by each cell $r_s A \Delta t$ is subtracted from the cell's state variable for assembled virions A and passed to the source term of the extracellular virus field (**T1**) to maintain mass balance.

E4 - Cell death

For cell death due to virally-induced apoptosis, each infected and virus-releasing cell can die due to the amount of intracellular viral. The rate of death is defined as a stochastic function of the state variable for assembled virions from the viral replication module (**E2**). If a virus releasing cell dies then it changes its cell type to dead and the cell's instances of the viral internalization, replication and release modules are disabled. The probability of virus-induced apoptosis per simulation step is a Hill equation of the current load of assembled virus,

$$\Pr(\tau(\sigma) \rightarrow Dead | \tau(\sigma) = Virus\ releasing) = \frac{\Delta t}{\alpha_{apo}} \frac{(A(\sigma))^{h_{apo}}}{(A(\sigma))^{h_{apo}} + V_{apo}{}^{h_{apo}}}, \tag{11}$$

where $A(\sigma)$ is the number of assembled virions in cell σ, h_{apo} is a Hill coefficient, V_{apo} is the amount of assembled virions at which the apoptosis probability is 0.5 per unit time and α_{apo} is a characteristic time constant of virally-induced apoptosis. For modeling of cell death due to contact cytotoxicity, see *I3 - Immune cell direct cytotoxicity and bystander effect*. For modeling of cell death due to oxidizing cytotoxicity, see *I4 - Immune cell oxidizing agent cytotoxicity*.

Lymph node modules

L1 - Immune cell recruitment

The total immune cell population is governed by an ordinary differential equation of a dimensionless state variable S that represents immune response due to local conditions and long-distance signaling. Our convention is that when $S > 0$, immune cells are recruited to the simulation domain; likewise, immune cells are removed from the simulation domain when $S < 0$. Probability functions of S describe the likelihood of immune cell seeding and removal,

$$\Pr(add\ immune\ cell) = erf(\alpha_{immune} S), \quad S > 0 \tag{12}$$

$$\Pr(remove\ immune\ cell) = erf(-\alpha_{immune} S), \quad S < 0 \tag{13}$$

Here the coefficient α_{immune} is the sensitivity of immune cell addition and removal to the state variable S. The dynamics of S are cast such that, in a homeostatic condition, a typical number of immune cells can be found in the simulation domain, and production of cytokine (**T2**) results in additional recruitment via long-distance signaling (*i.e.*, with some delay). We model this homeostatic feature using the feedback mechanism of the total number of immune cells N_{immune} in the simulation domain. Cytokine signaling is modeled as perturbing the homeostatic state using the term $\alpha_{sig}\delta$. Here δ is the total amount of decayed cytokine in the simulation domain

and $\alpha_{sig} > 0$ models signaling by transmission of cytokine to some far-away source of immune cells. We write the rate of change of S as

$$\frac{dS}{dt} = \beta_{add} - \beta_{sub} N_{immune} + \frac{\alpha_{sig}}{\beta_{delay}} \delta - \beta_{decay} S. \tag{14}$$

Here β_{add} and β_{sub} control the number of immune cells in the simulation domain under homeostatic conditions. β_{delay} controls the delay between transmission of the cytokine to the lymph node and corresponding immune response by adjusting the rate of recruitment due to total cytokine (*i.e.*, increasing β_{delay} increases the resulting delay). β_{decay} regulates the return of S to an unperturbed state (*i.e.*, $S = 0$, increasing β_{decay} increases the rate of return to $S = 0$). To determine the seeding location, the simulation space is randomly sampled $n_{seeding}$ times, and an immune cell is seeded at the unoccupied location with the highest amount of the virus field. If no location is unoccupied, then the immune cell is not seeded. The removal probability is evaluated for each immune cell at each simulation step. Immune cells are removed by setting their volume constraint to zero.

Immune cell modules

The four processes **I1**-**I4** capture immune cell functions which are defined below. These processes control how immune cells are activated, translocate, and kill other cells. Their interactions with epithelial cells and other model components are illustrated in Figure 15.

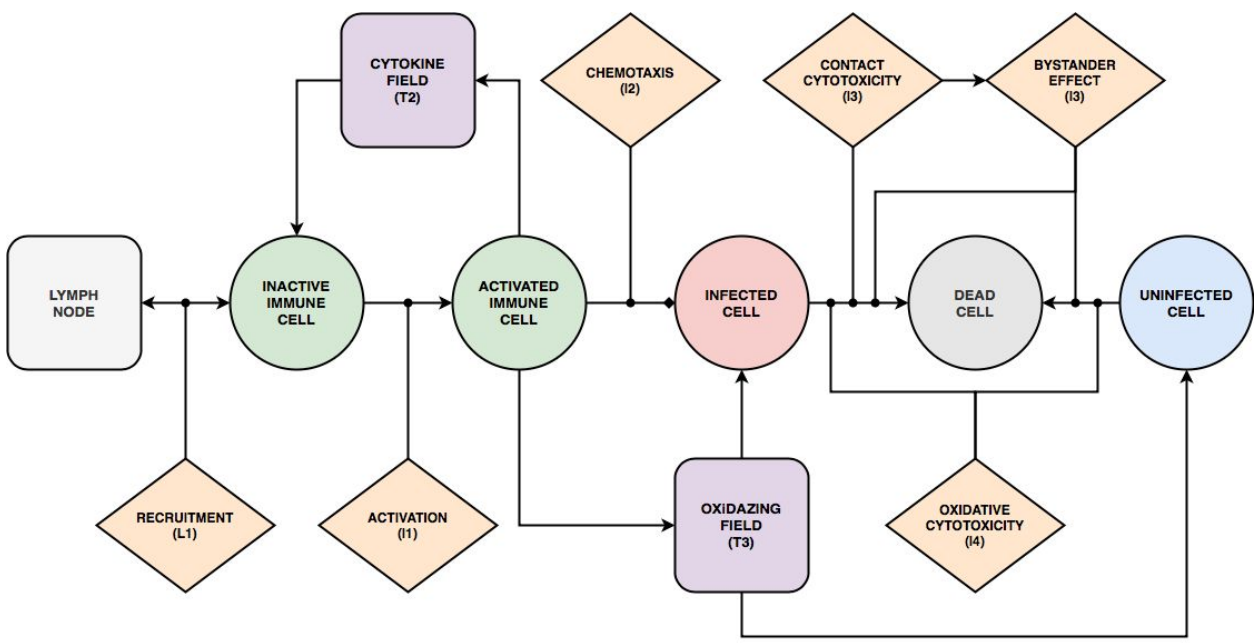

Figure 15. State diagram and interactions of Immune cells. Immune cells can adopt two different generalized types: inactive and activated. Inactive immune cells are recruited by the cytokine levels according to the immune recruitment module (**L1**).Transition from inactive to activated immune cells is determined by the immune activation module (**I1**) when cells are exposed to cytokines in the tissue. Activated immune cells amplify the cytokine signal by

secreting cytokines to the extracellular environment. Activated immune cells chemotax towards virus-releasing cells (**I2**). Immune cells induce death of epithelial cells by direct cytotoxicity when coming into contact with infected cells (**I3**), bystander effect by killing neighbors of infected cells (**I3**) and through oxidative cytotoxicity (**I4**) by releasing cytotoxic oxidizing agents (**T3**) into the extracellular environment.

I1 - Immune cell activation

Inactive immune cells become activated with a probability according to a Hill equation of the total cytokine bound to the cell $B_{cyt}(\sigma,\ t)$,

$$\Pr(\tau(\sigma,\ t) \rightarrow activated\ immune | \tau(\sigma,\ t) = inactive\ immune) = \frac{\left(B_{cyt}(\sigma,\ t)\right)^{h_{act}}}{\left(B_{cyt}(\sigma,\ t)\right)^{h_{act}} + V_{act}{}^{h_{act}}}. \tag{15}$$

After one hour, an activated immune cell becomes inactive, in which case evaluations of activation (Equation (15)) recommence. The immune cells "forget" a percentage ($1 - \rho_{cyt}$) of the bound cytokine each time step while taking up an amount of cytokine from the environment ($\omega_{cyt}(\tau(\sigma),\ t)$ defined in **T2**),

$$B_{cyt}(\sigma,\ t) = \rho_{cyt} B_{cyt}(\sigma,\ t - \Delta t) + \omega_{cyt}(\tau(\sigma(x)),\ t). \tag{16}$$

I2 - Immune cell chemotaxis

Activated immune cells experience a motile force as a response to a signaling field. Immune cells chemotax along concentration gradients of the cytokine field. The chemotactic effective energy $\mathcal{H}_{chemotaxis}$ associated with the gradient is calculated according to a chemotactic sensitivity parameter $\lambda_{chemotaxis}$ and calculated chemotactic force $F_{chemotaxis}$. The contribution of $\mathcal{H}_{chemotaxis}$ to the change in the system's total effective energy is calculated using $F_{chemotaxis}$ when considering copy attempts. The chemotactic force at a location x is saturated by normalizing the chemotactic sensitivity parameter by the concentration of cytokine at the center of mass of the cell at x, $c_{cyt,\ CM}(\sigma(x))$,

$$F_{chemotaxis}(x) = \frac{\lambda_{chemotaxis}}{1 + c_{cyt,\ CM}(\sigma(x))} \nabla c_{cyt}(x). \tag{17}$$

I3 - Immune cell direct cytotoxicity and bystander effect

Immune cells, whether activated or not, have the ability to kill infected cells by direct contact. At each simulation step, neighbors of infected cells are evaluated. Immune cells trigger cell death in the infected and virus-releasing epithelial cells in which they come in contact. When an infected cell is killed by direct cytotoxicity, each of its first order neighbors is evaluated for cell death by a bystander effect. Each neighbor has a probability of dying from bystander effect $k_{bystander}$:

$$\Pr(\tau(\sigma) \rightarrow Dead | Neighbor(\sigma)\ Direct\ Cytotoxicity\ =\ True) = k_{bystander}. \tag{18}$$

I4 - Immune cell oxidizing agent cytotoxicity

Immune cells release a short-range, diffusive oxidizing agent when exposed to high cytokine concentration (**T3**). The oxidizing agent kills an epithelial cell of any type when the total amount of oxidizing agent in the domain of the cell exceeds a threshold for death, τ_{oxi}^{death}.

Extracellular environment modules

T1 - Viral transport

The change in concentration of the virus field c_{vir} is calculated at each location in the simulation domain by solving the following reaction-diffusion equation,

$$\frac{\partial c_{vir}(x)}{\partial t} = D_{vir}\Delta c_{vir}(x) - \gamma_{vir}c_{vir}(x) + \frac{1}{v(\sigma(x))}\left(Release(\sigma(x)) - Uptake(\sigma(x))\right). \tag{19}$$

Here D_{vir} is the diffusion constant of the extracellular virus and γ_{vir} is the decay rate is the decay rate. Uptake and release by a cell at each location are determined using the viral internalization (**E1**) and the viral release (**E3**) modules, and are uniformly applied over all sites of the domain of the cell.

T2 - Cytokine transport

The change in concentration of the cytokine field c_{cyt} is obtained by solving a reaction-diffusion equation of the following general form,

$$\frac{\partial c_{cyt}}{\partial t} = D_{cyt}\Delta c_{cyt} - \gamma_{cyt}c_{cyt} + s_{cyt}. \tag{20}$$

The decay term $\gamma_{cyt}c_{cyt}$ represents cytokine leaving the simulation domain (*e.g.*, in immune recruitment). To model immune signaling, cytokine secretion is described by a Hill equation according to cell type and the total amount of a field (extracellular virus or cytokine) inside the domain of a cell,

$$s_{cyt}(x) = \sigma_{cyt}(\tau(\sigma(x)))\frac{\left(c_{sig}(\sigma(x))\right)^2}{\left(c_{sig}(\sigma(x))\right)^2 + V_{cyt}^{\ 2}} - \omega_{cyt}(\tau(\sigma(x))). \tag{21}$$

Here $\sigma_{cyt}(\tau(\sigma(x)))$ is the maximum cytokine secretion rate by cell type at x, $c_{sig}(\sigma(x))$ is a quantity that affects its cytokine secretion, $\omega_{cyt}(\tau(\sigma(x)))$ is the cytokine uptake rate of the cell type at x and V_{cyt} is a dissociation coefficient of cytokine secretion. σ_{cyt} is nonzero for infected epithelial cells, virus-releasing epithelial cells and activated immune cells. c_{sig} for infected and virus-releasing epithelial cells is the amount of assembled virus A in the viral replication

module, and for activated immune cells c_{sig} is the total amount of cytokine in the domain of the cell. $\omega_{cyt}(\tau(\sigma(x)))$ is constant and nonzero for activated and inactive immune cells.

T3 - Oxidizing agent transport

The oxidizing agent field diffuses according to the reaction-diffusion equation,

$$\frac{\partial c_{oxi}}{\partial t} = D_{oxi}\Delta c_{oxi} - \gamma_{oxi}c_{oxi} + s_{oxi}. \tag{22}$$

Bursts of oxidizing agent are implemented as a source term for one time step according to a rate coefficient σ_{oxi}, which is uniformly mapped onto the source term s_{oxi} over the domain of each activated immune cell. An oxidizing burst occurs in immune cells with an activated state when the total cytokine in the immune cell's domain exceeds a threshold τ_{oxi}^{sec}.

Initial and boundary conditions

The domain of all simulations had dimensions of 90 x 90 x 2 lattice sites. The initial cell configuration consisted of a 30 x 30 sheet of uninfected epithelial cells, each of size 3 x 3, on the lower layer of lattice sites. Epithelial cells were "frozen", in that they were immobile, leaving the remaining 90 x 90 subdomain for occupancy by recruited immune cells. For cellular dynamics and mass transport, periodic boundary conditions were applied in the plane of the epithelial sheet, and Neumann conditions were applied along the direction orthogonal to the epithelial sheet. All field solutions for the diffusive viral, cytokine and oxidizing agent fields were initialized as zero everywhere.

At each first simulation step, the epithelial cell in the center of the sheet was set to infected, and its unpacking state variable U of the viral replication model was set to a value of one. All epithelial cells were initialized with a number of unbound surface receptors $SR = R_o$. All immune cells, when introduced to the simulation by recruitment, were initialized in an inactive state, and with a bound cytokine value equal to zero ($B_{cyt} = 0$). During transition of an uninfected epithelial cell to the infected type, all state variables of the viral replication model were initialized with a value of zero.

Simulation specifications

Model implementation and all simulations were performed using CompuCell3D, which uses a non-dimensional lattice for CPM-based cellular dynamics and non-dimensional explicit time integration of reaction-diffusion field solutions. As such, a baseline parameter set was constructed for all CPM parameters and modules developed in this work (Table 1). Non-dimensionalization was performed on model parameters for a lattice dimension of 4 μm per pixel along each dimension, at 20 minutes (1/3 hours) per MCS. All replicas were simulated for

ten trials, each 1,000 MCS (20000 minutes, 333 hours, 14 days) long. Simulation data was collected at a frequency of 10 MCSs (200 minutes, 3 hours) for all simulations.

Table 1. Parameter values in baseline parameter set.

Conversion Factors	Value
Simulation step Δt	1200.0 s
Lattice width	4.0 μm
Scale factor for concentration	1×10^{-14} mol
Simulation parameters	**Value**
Cell diameter	12.0 μm
Replication rate r_{max}	$1/12\times10^{-3}$ s^{-1}
Translating rate r_t	$1/18\times10^{-3}$ s^{-1}
Unpacking rate r_u	$1/6\times10^{-3}$ s^{-1}
Packaging rate r_p	$1/6\times10^{-3}$ s^{-1}
Release rate r_s	$1/6\times10^{-3}$ s^{-1}
Scale factor for number of mRNA per infected cell $mRNA_{avg}$	1000 $cell^{-1}$
Viral dissociation coefficient r_{half}	2000
Viral diffusion coefficient D_{vir}	0.01 $\mu m^2/s$
Viral diffusion length λ_{vir}	36 μm
Viral decay rate γ_{vir}	7.71×10^{-6} s^{-1}
Cytokine diffusion coefficient D_{cyt} (IL-2 cytokine) [54,55]	0.16 $\mu m^2/s$
Cytokine diffusion length λ_{cyt} (IL-2 cytokine) [54]	100 μm
Cytokine decay rate γ_{cyt} (IL-2 cytokine) [derived from lambda and D]	1.32×10^{-5} s^{-1}
Maximum cytokine immune secretion rate $\sigma_{cyt}(immune\ activated)$ [used 1/10 of infected secretion rate]	3.5×10^{-4} pM/s
Immune secretion midpoint [55]	1 pM
Cytokine immune uptake rate $\omega_{cyt}(immune\ activated)$ [54]	3.5×10^{-5} pM/s
Maximum cytokine infected cell secretion rate $\sigma_{cyt}(infected)$ [54]	3.5×10^{-3} pM/s
Infected cell cytokine secretion mid-point	0.1 pM
Immune cell cytokine activation $EC50_{cyt,\,act}$	1 pM

Immune cell equilibrium bound cytokine EQ_{ck}	134.4 pM
Immune cell bound cytokine memory ρ_{cyt}	0.98 s^{-1}
Immune cell activated time	10 h
Oxidation Agent diffusion coefficient D_{oxi}	0.64 $\mu m^2/s$
Oxidation Agent diffusion length λ_{oxi}	36 μm
Oxidation Agent decay rate γ_{oxi}	1.32×10^{-5} s^{-1}
Immune cell oxidation agent secretion rate σ_{oxi}	3.5×10^{-3} pM/s
Immune cell C_{cyt} threshold for Oxidation Agent release τ_{oxi}^{sec}	10 pM
Tissue cell C_{oxi} threshold for death τ_{oxi}^{death}	1.5 pM
Initial density of unbound cell surface receptors R_o	200 $cell^{-1}$
Virus-receptor association affinity k_{on}	1.4×10^{4} $M^{-1}s^{-1}$
Virus-receptor dissociation affinity k_{off}	1.4×10^{-4} s^{-1}
Infection threshold	1
Uptake Hill coefficient h_{upt}	2
Uptake characteristic time constant α_{upt}	20 min
Virally-induced apoptosis Hill coefficient h_{apo}	2
Virally-induced apoptosis dissociation coefficient V_{apo}	100×10^{-14} mol
Virally-induced apoptosis characteristic time constant α_{apo}	20 min
Immune cell activation Hill coefficient h_{act}	2
Immune cell activation dissociation coefficient V_{act}	64×10^{-14} mol
Immune response add immune cell coefficient β_{add}	1/1200 s^{-1}
Immune response subtract immune cell coefficient β_{sub}	1/6000 $cell^{-1}s^{-1}$
Immune response delay coefficient β_{delay}	3000 s
Immune response decay coefficient β_{decay}	1/12000 s^{-1}
Immune response cytokine transmission coefficient α_{sig}	0.5
Immune response probability scaling coefficient α_{immune}	0.01
Number of immune cell seeding samples $n_{seeding}$	10
Initial target volume	64 μm^3
Lambda volume λ_{volume}	9

Initial number of immune cells	0
Lambda chemotaxis $\lambda_{chemotaxis}$	1
Intrinsic Random Motility $\mathcal{M}^*$	10
Contact coefficients J (all interfaces)	10

References

1. Cao Y-C, Deng Q-X, Dai S-X. Remdesivir for severe acute respiratory syndrome coronavirus 2 causing COVID-19: An evaluation of the evidence. Travel Med Infect Dis. 2020; 101647–101647. doi:10.1016/j.tmaid.2020.101647
2. Wang D, Yin Y, Hu C, Liu X, Zhang X, Zhou S, et al. Clinical course and outcome of 107 patients infected with the novel coronavirus, SARS-CoV-2, discharged from two hospitals in Wuhan, China. Critical Care. 2020;24: 188. doi:10.1186/s13054-020-02895-6
3. Eckhardt M, Hultquist JF, Kaake RM, Hüttenhain R, Krogan NJ. A systems approach to infectious disease. Nature Reviews Genetics. 2020;21: 339–354. doi:10.1038/s41576-020-0212-5
4. Dolley S. Big Data's Role in Precision Public Health. Front Public Health. 2018;6: 68–68. doi:10.3389/fpubh.2018.00068
5. Garira W. A primer on multiscale modelling of infectious disease systems. Infectious Disease Modelling. 2018;3: 176–191. doi:10.1016/j.idm.2018.09.005
6. Wang Y, Heiland R, Craig M, Davis C, Ford Versypt AN, Jenner A, et al. Rapid community-driven development of a SARS-CoV-2 tissue simulator. bioRxiv. 2020; 2020.04.02.019075. doi:10.1101/2020.04.02.019075
7. Hernandez Vargas EA, Velasco-Hernandez JX. In-host Modelling of COVID-19 Kinetics in Humans. medRxiv. 2020; 2020.03.26.20044487. doi:10.1101/2020.03.26.20044487
8. Koelle K, Farrell AP, Brooke CB, Ke R. Within-host infectious disease models accommodating cellular coinfection, with an application to influenza†. Virus Evolution. 2019;5. doi:10.1093/ve/vez018
9. Keef E, Zhang LA, Swigon D, Urbano A, Ermentrout GB, Matuszewski M, et al. Discrete dynamical modeling of influenza virus infection suggests age-dependent differences in immunity. García-Sastre A, editor. J Virol. 2017;91: e00395-17. doi:10.1128/JVI.00395-17
10. Dee KU, Hammer DA, Shuler ML. A model of the binding, entry, uncoating, and RNA synthesis of Semliki Forest virus in baby hamster kidney (BHK-21) cells. Biotechnology and Bioengineering. 1995;46: 485–496. doi:10.1002/bit.260460513
11. English TJ, Hammer DA. Brownian adhesive dynamics (BRAD) for simulating the receptor-mediated binding of viruses. Biophys J. 2004;86: 3359–3372. doi:10.1529/biophysj.103.027813
12. Boireau S, Maiuri P, Basyuk E, de la Mata M, Knezevich A, Pradet-Balade B, et al. The transcriptional cycle of HIV-1 in real-time and live cells. J Cell Biol. 2007;179: 291–304. doi:10.1083/jcb.200706018
13. Roldão A, Vieira HLA, Charpilienne A, Poncet D, Roy P, Carrondo MJT, et al. Modeling rotavirus-like particles production in a baculovirus expression vector system: Infection kinetics, baculovirus DNA replication, mRNA synthesis and protein production. Journal of Biotechnology. 2007;128: 875–894. doi:10.1016/j.jbiotec.2007.01.003
14. Purohit PK, Inamdar MM, Grayson PD, Squires TM, Kondev J, Phillips R. Forces during bacteriophage DNA packaging and ejection. Biophys J. 2004/11/19. 2005;88: 851–866. doi:10.1529/biophysj.104.047134
15. Yang Q, Catalano CE. A minimal kinetic model for a viral DNA packaging machine. Biochemistry. 2004;43: 289–299. doi:10.1021/bi035532h
16. Baltimore D. Expression of animal virus genomes. Bacteriol Rev. 1971;35: 235–241.
17. Dahari H, Ribeiro RM, Rice CM, Perelson AS. Mathematical modeling of subgenomic

hepatitis C virus replication in Huh-7 cells. J Virol. 2007;81: 750. doi:10.1128/JVI.01304-06
18. Regoes RR, Crotty S, Antia R, Tanaka MM. Optimal Replication of Poliovirus within Cells. The American Naturalist. 2005;165: 364–373. doi:10.1086/428295
19. Baccam P, Beauchemin C, Macken CA, Hayden FG, Perelson AS. Kinetics of influenza A virus Infection in humans. J Virol. 2006;80: 7590. doi:10.1128/JVI.01623-05
20. Sidorenko Y, Reichl U. Structured model of influenza virus replication in MDCK cells. Biotechnology and Bioengineering. 2004;88: 1–14. doi:10.1002/bit.20096
21. Zhdanov VP. Kinetic model of HIV infection. J Exp Theor Phys. 2007;105: 856–860. doi:10.1134/S1063776107100202
22. Reddy B, Yin J. Quantitative Intracellular Kinetics of HIV Type 1. AIDS Research and Human Retroviruses. 1999;15: 273–283. doi:10.1089/088922299311457
23. Nakabayashi J, Sasaki A. The function of temporally ordered viral gene expression in the intracellular replication of herpes simplex virus type 1 (HSV-1). J Theor Biol. 2009;261: 156–164. doi:10.1016/j.jtbi.2009.07.035
24. Nakabayashi J, Sasaki A. A mathematical model of the intracellular replication and within host evolution of hepatitis type B virus: Understanding the long time course of chronic hepatitis. J Theor Biol. 2011;269: 318–329. doi:10.1016/j.jtbi.2010.10.024
25. Taubenberger JK, Morens DM. The pathology of influenza virus infections. Annu Rev Pathol. 2008;3: 499–522. doi:10.1146/annurev.pathmechdis.3.121806.154316
26. Strain MC, Richman DD, Wong JK, Levine H. Spatiotemporal Dynamics of HIV Propagation. Journal of Theoretical Biology. 2002;218: 85–96. doi:10.1006/jtbi.2002.3055
27. Bocharov G, Meyerhans A, Bessonov N, Trofimchuk S, Volpert V. Spatiotemporal Dynamics of Virus Infection Spreading in Tissues. PLOS ONE. 2016;11: e0168576. doi:10.1371/journal.pone.0168576
28. Koullapis PG, Stylianou FS, Sznitman J, Olsson B, Kassinos SC. Towards whole-lung simulations of aerosol deposition: A model of the deep lung. J Aerosol Sci. 2020;144: 105541. doi:10.1016/j.jaerosci.2020.105541
29. Graw F, Perelson A. Spatial aspects of HIV infection. 2013. pp. 3–31. doi:10.1007/978-1-4614-4178-6_1
30. Immonen T, Gibson R, Leitner T, Miller M, Arts E, Somersalo E, et al. A hybrid stochastic-deterministic computational model accurately describes spatial dynamics and virus diffusion in HIV-1 growth competition assay. Journal of theoretical biology. 2012;312C: 120–132. doi:10.1016/j.jtbi.2012.07.005
31. Zorzenon dos Santos RM, Coutinho S. Dynamics of HIV Infection: A cellular automata approach. Phys Rev Lett. 2001;87: 168102. doi:10.1103/PhysRevLett.87.168102
32. Imle A, Kumberger P, Schnellbächer ND, Fehr J, Carrillo-Bustamante P, Ales J, et al. Experimental and computational analyses reveal that environmental restrictions shape HIV-1 spread in 3D cultures. Nat Commun. 2019;10: 2144. doi:10.1038/s41467-019-09879-3
33. Beauchemin C. Probing the effects of the well-mixed assumption on viral infection dynamics. J Theor Biol. 2006;242: 464–477. doi:10.1016/j.jtbi.2006.03.014
34. Myers MA, Smith AP, Lane LC, Moquin DJ, Vogel P, Woolard S, et al. Dynamically linking influenza virus infection with lung injury to predict disease severity. bioRxiv. 2019; 555276. doi:10.1101/555276
35. Carrasco Pro S, Dafonte Imedio A, Santoso CS, Gan KA, Sewell JA, Martinez M, et al. Global landscape of mouse and human cytokine transcriptional regulation. Nucleic Acids Research. 2018;46: 9321–9337. doi:10.1093/nar/gky787
36. Akira S, Uematsu S, Takeuchi O. Pathogen Recognition and Innate Immunity. Cell.

2006;124: 783–801. doi:10.1016/j.cell.2006.02.015
37. Ahlquist P, Noueiry AO, Lee W-M, Kushner DB, Dye BT. Host Factors in Positive-Strand RNA Virus Genome Replication. J Virol. 2003;77: 8181. doi:10.1128/JVI.77.15.8181-8186.2003
38. Edelblum KL, Turner JR. Chapter 12 - Epithelial cells: structure, transport, and barrier function. In: Mestecky J, Strober W, Russell MW, Kelsall BL, Cheroutre H, Lambrecht BN, editors. Mucosal Immunology (Fourth Edition). Boston: Academic Press; 2015. pp. 187–210. doi:10.1016/B978-0-12-415847-4.00012-4
39. Rosendahl Huber S, van Beek J, de Jonge J, Luytjes W, van Baarle D. T cell responses to viral infections - opportunities for Peptide vaccination. Front Immunol. 2014;5: 171–171. doi:10.3389/fimmu.2014.00171
40. Le Page C, Génin P, Baines M, Hiscott J. Interferon activation and innate immunity. Rev Immunogenet. 2000;2: 374–386.
41. Abbas AK, Lichtman AH, Pillai S. Cellular and molecular immunology. 9th ed. Philadelphia, PA: Saunders/Elsevier; 2017.
42. Ploquin A, Zhou Y, Sullivan NJ. Ebola Immunity: Gaining a Winning Position in Lightning Chess. JI. 2018;201: 833–842. doi:10.4049/jimmunol.1700827
43. Yin J, Redovich J. Kinetic Modeling of Virus Growth in Cells. Microbiol Mol Biol Rev. 2018;82: e00066-17. doi:10.1128/MMBR.00066-17
44. Yu X, Zeng X, Shi W, Hu Y, Nie W, Chu N, et al. Validation of Cycloserine Efficacy in Treatment of Multidrug-Resistant and Extensively Drug-Resistant Tuberculosis in Beijing, China. Antimicrobial Agents and Chemotherapy. 2018;62. doi:10.1128/AAC.01824-17
45. Swat MH, Thomas GL, Belmonte JM, Shirinifard A, Hmeljak D, Glazier JA. Multi-scale modeling of tissues using CompuCell3D. Methods Cell Biol. 2012;110: 325–366. doi:10.1016/B978-0-12-388403-9.00013-8
46. Cheng AH-D, Cheng DT. Heritage and early history of the boundary element method. Eng Anal Bound Elem. 2005;29: 268–302. doi:10.1016/j.enganabound.2004.12.001
47. Zhao X, Wang W. Fisher waves in an epidemic model. Discrete Cont Dyn-B. 2004;4: 1117–1128. doi:10.3934/dcdsb.2004.4.1117
48. Warren TK, Jordan R, Lo MK, Ray AS, Mackman RL, Soloveva V, et al. Therapeutic efficacy of the small molecule GS-5734 against Ebola virus in rhesus monkeys. Nature. 2016/03/02. 2016;531: 381–385. doi:10.1038/nature17180
49. Mirams GR, Arthurs CJ, Bernabeu MO, Bordas R, Cooper J, Corrias A, et al. Chaste: an open source C++ library for computational physiology and biology. PLoS Comput Biol. 2013;9: e1002970. doi:10.1371/journal.pcbi.1002970
50. Pitt-Francis J, Pathmanathan P, Bernabeu MO, Bordas R, Cooper J, Fletcher AG, et al. Chaste: A test-driven approach to software development for biological modelling. Comput Phys Commun. 2009;180: 2452–2471. doi:10.1016/j.cpc.2009.07.019
51. Starruß J, de Back W, Brusch L, Deutsch A. Morpheus: a user-friendly modeling environment for multiscale and multicellular systems biology. Bioinformatics. 2014;30: 1331–1332. doi:10.1093/bioinformatics/btt772
52. Smith LP, Bergmann FT, Chandran D, Sauro HM. Antimony: a modular model definition language. Bioinformatics. 2009/07/03. 2009;25: 2452–2454. doi:10.1093/bioinformatics/btp401
53. Graner F, Glazier JA. Simulation of biological cell sorting using a two-dimensional extended Potts model. Phys Rev Lett. 1992;69: 2013–2016. doi:10.1103/PhysRevLett.69.2013
54. Oyler-Yaniv A, Oyler-Yaniv J, Whitlock BM, Liu Z, Germain RN, Huse M, et al. A tunable diffusion-consumption mechanism of cytokine propagation enables plasticity in cell-to-cell

communication in the immune system. Immunity. 2017;46: 609–620. doi:10.1016/j.immuni.2017.03.011
55. Höfer T, Krichevsky O, Altan-Bonnet G. Competition for IL-2 between regulatory and effector T cells to chisel immune responses. Front Immunol. 2012;3: 268–268. doi:10.3389/fimmu.2012.00268

Acknowledgments

We would like to thank Ramray Bhat, Ryan Danehy, Javier Toledo, Bard Ermentrout, Geoffrey Fox, Yi Jiang, Paul Macklin, Jairaj Mathur, Roeland Merks, Ericka Mochan, Jason Shoemaker and Amber Smith for useful discussions and ideas and for comments on the manuscript. JAG, TJS, JFG and JAS acknowledge funding from National Institutes of Health grants U24 EB028887 and R01 GM122424 and National Science Foundation grant NSF 1720625. LB acknowledges grant 01ZX1707A within the German e:Med initiative (BMBF) and grant 391070520 from the German Research Foundation (DFG). R.K.P. was supported, in part, by National Institutes of Health grants R01 AI071002, R01 AI141222 and R01 HD079327. The funders had no role in manuscript preparation or the decision to submit the work for publication.

Competing Interests

JAG is the owner/operator of Virtual Tissues for Health, LLC, which develops applications of multiscale tissue models in medical applications and is a shareholder in Gilead Life Sciences.

Supplementary Materials

Spatial configuration panels

No immune system

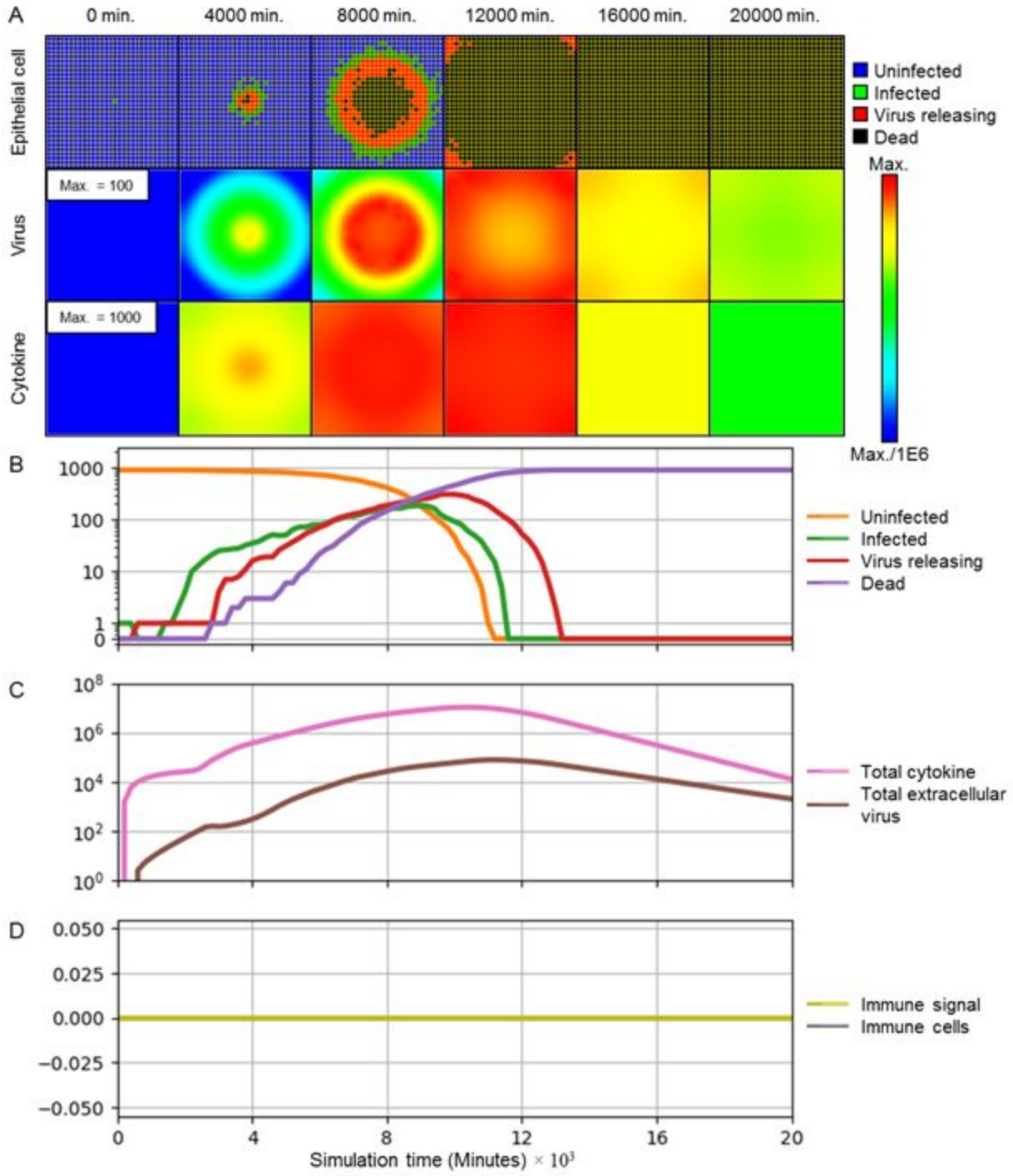

Figure S1. Simulation of the progression of infection in a patch of epithelial tissue, with all parameters as in Figure 3, but with no cellular immune system response corresponding to virus spread in an *in vitro* or organoid culture, or a severely immunosuppressed individual. **A**. Snapshots of spatial configuration *vs* time showing progression of simulated infection. Columns, left to right: 0 minutes (time of initial infection), 4000 minutes (67 hours, 2 ¾ days) after infection, 8000 minutes (133 hours, 5 ½ days), 12000 minutes (200 hours, 8 ⅓ days), 16000 minutes (267 hours, 11 days), and 20000 minutes (333 hours, 14 days). First row: epithelial cell layer composed of uninfected (blue), infected (green), virus releasing (red) cells and dead cells (black). Second row: level of extracellular virus field. Third row: extracellular cytokine field. Fields are color-coded on a logarithmic scale: red

corresponds to the chosen maximum value specified in the first panel, blue to six orders of magnitude lower than the maximum value, and values outside this range are colored as their closest border value. **B-D**. Simulation time series. **B**. Number of uninfected (orange), infected (green), virus releasing (red) and dead (purple) epithelial cells on a logarithmic scale *vs* time *vs* time in minutes. **C**. Total extracellular cytokine (magenta) and total extracellular virus (brown) on a logarithmic scale *vs* time in minutes. **D**. Value of the immune recruitment signal S (yellow) and number of immune cells (grey) on a linear scale *vs* time in minutes.

Special cases of classifications of spatiotemporal dynamics

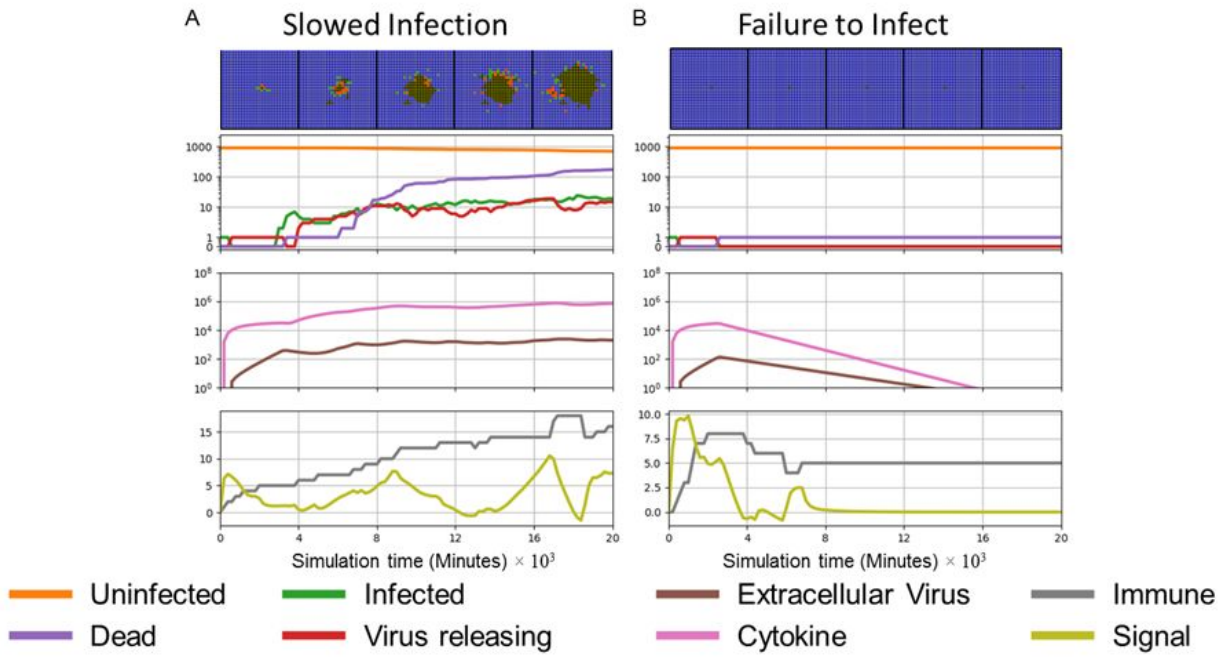

Figure S2. Special cases of spatiotemporal infection dynamics. **A**. A border case of slowed infection towards containment is Slowed Infection with constant virus: when the net effectiveness of viral and immune dynamics are balanced, the number of infected cells and the total extracellular virus fluctuate around steady state levels. **B**. A limit case of Clearance is the failure to infect: initially infected cells may replicate and secrete virus, but insufficiently so to infect other cells during simulation time such that any initially infected cells vanish and total extracellular virus drops below a threshold of 10^{-3} per cell area.

Parameter values for Figure 4

Parameter	No immune response	Widespread infection	Slowed infection	Containment	Recurrence	Clearance
Virus-receptor association affinity k_{on} ($M^{-1}s^{-1}$)	1.4×10^4	1.4×10^4	1.4×10^3	1.4×10^2	1.4×10^6	1.4×10^4

Immune response delay coefficient β_{delay} (s)	-	30000	300000	300	30	300

Table S1. Varying parameters in simulations shown in Figure 4. Virus-receptor association affinity and immune response delay coefficient shown for no immune response (Figure 4A), widespread infection (Figure 4B), slowed infection (Figure 4C), containment (Figure 4D), recurrence (Figure 4E) and clearance (Figure 4F). All other parameters are as in Table 1.

Sweep of immune response delay β_{delay} and virus-receptor association affinity k_{on}

Dead cells

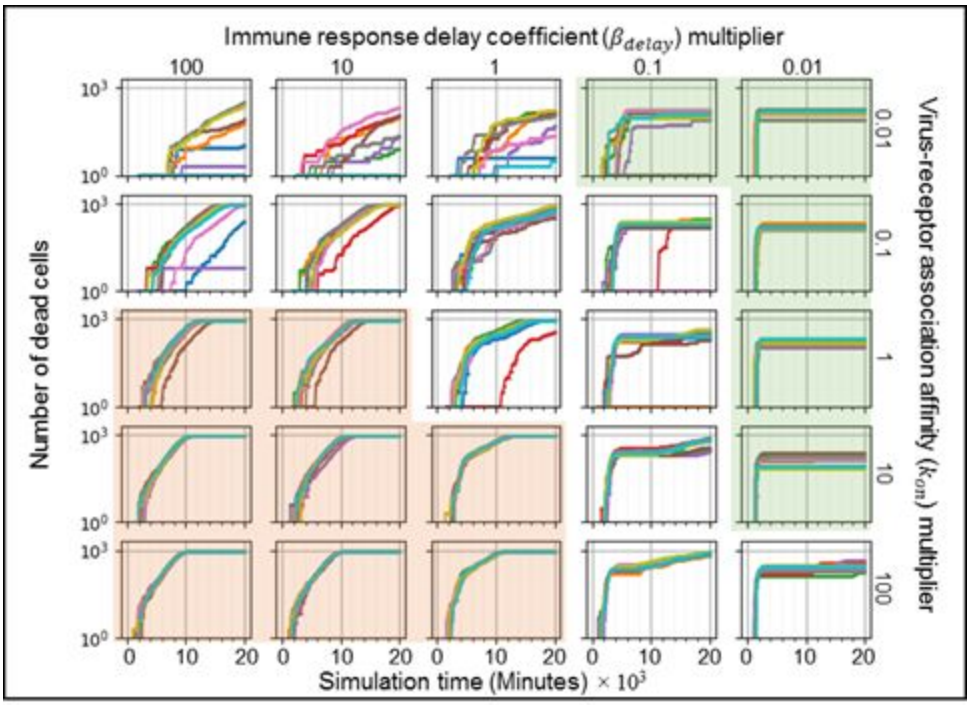

Figure S3. Time series of the number of uninfected cells for simulations in Figure 5. Logarithmic multidimensional parameter sweep performed by running 10 simulation replicas increasing and decreasing the baseline parameter values 10-fold and 100-fold for all parameter sets and replicas in Figure 5. Results show consistent containment/clearance for small k_{on} and smal β_{delay} (upper right, green-shaded subplots), widespread infection for high k_{on} and smal β_{delay} (lower left, orange-shaded subplots), and multiple outcomes for the same parameter values (uncolored subplots). Number of cells are shown on a logarithmic scale *vs* time in minutes.

Virus releasing cells

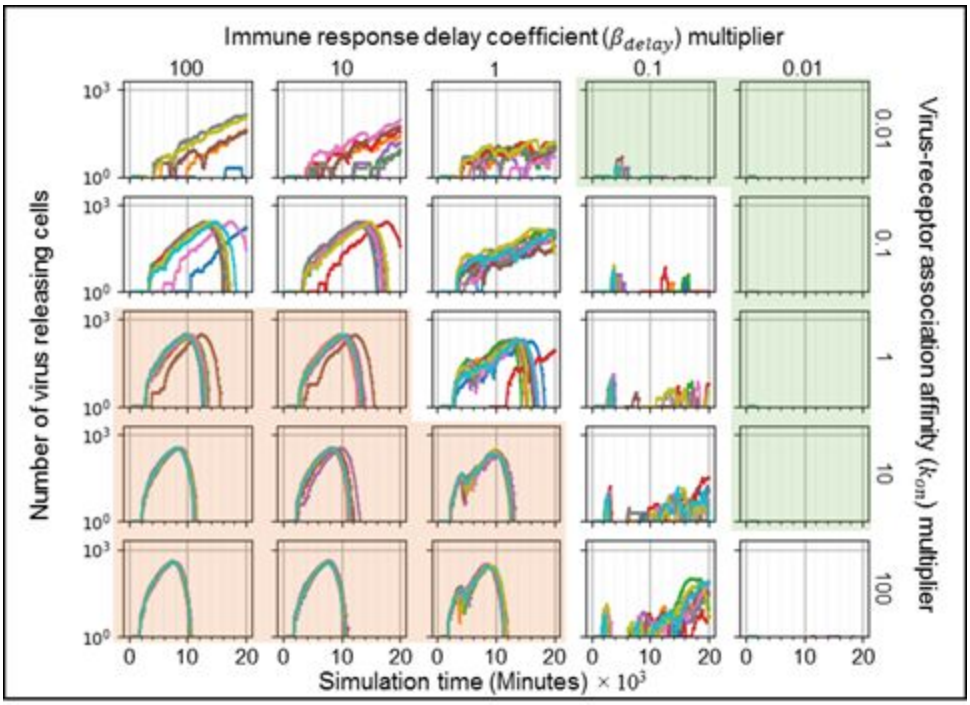

Figure S4. Time series of the number of virus releasing cells for simulations in Figure 5. Logarithmic multidimensional parameter sweep performed by running 10 simulation replicas increasing and decreasing the baseline parameter values 10-fold and 100-fold for all parameter sets and replicas in FIgure 5. Results show consistent containment/clearance for small k_{on} and smal β_{delay} (upper right, green-shaded subplots), widespread infection for high k_{on} and smal β_{delay} (lower left, orange-shaded subplots), and multiple outcomes for the same parameter values (uncolored subplots). Number of cells are shown on a logarithmic scale *vs* time in minutes.

Immune cells

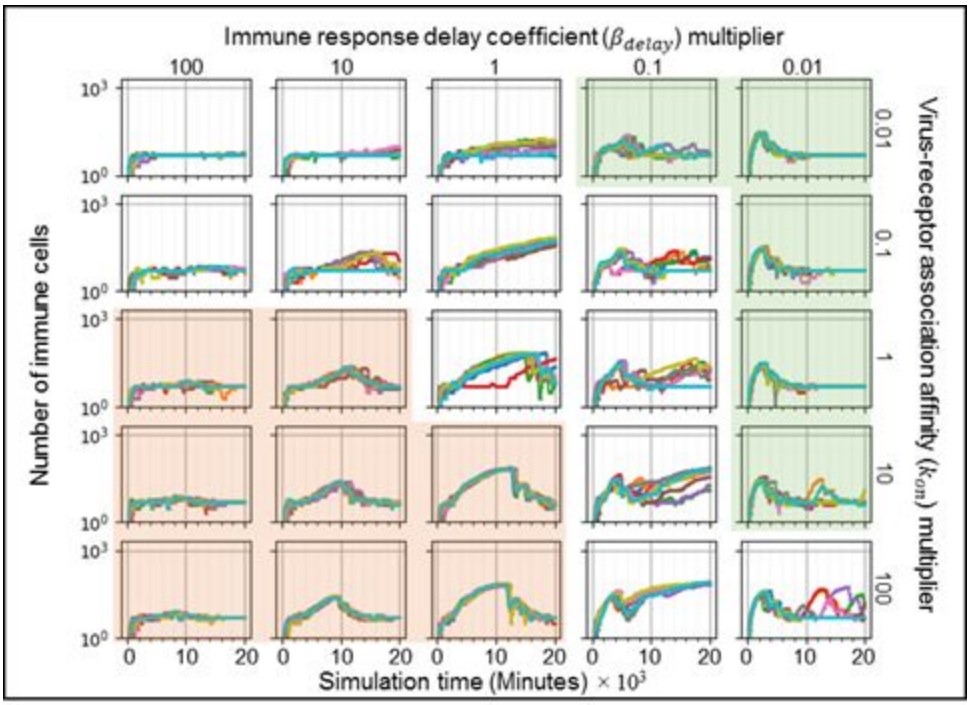

Figure S5. Time series of the number of immune cells for simulations in Figure 5. Logarithmic multidimensional parameter sweep performed by running 10 simulation replicas increasing and decreasing the baseline parameter values 10-fold and 100-fold for all parameter sets and replicas in FIgure 5. Results show consistent containment/clearance for small k_{on} and smal β_{delay} (upper right, green-shaded subplots), widespread infection for high k_{on} and smal β_{delay} (lower left, orange-shaded subplots), and multiple outcomes for the same parameter values (uncolored subplots). Number of cells are shown on a logarithmic scale *vs* time in minutes.

Immune response state variable

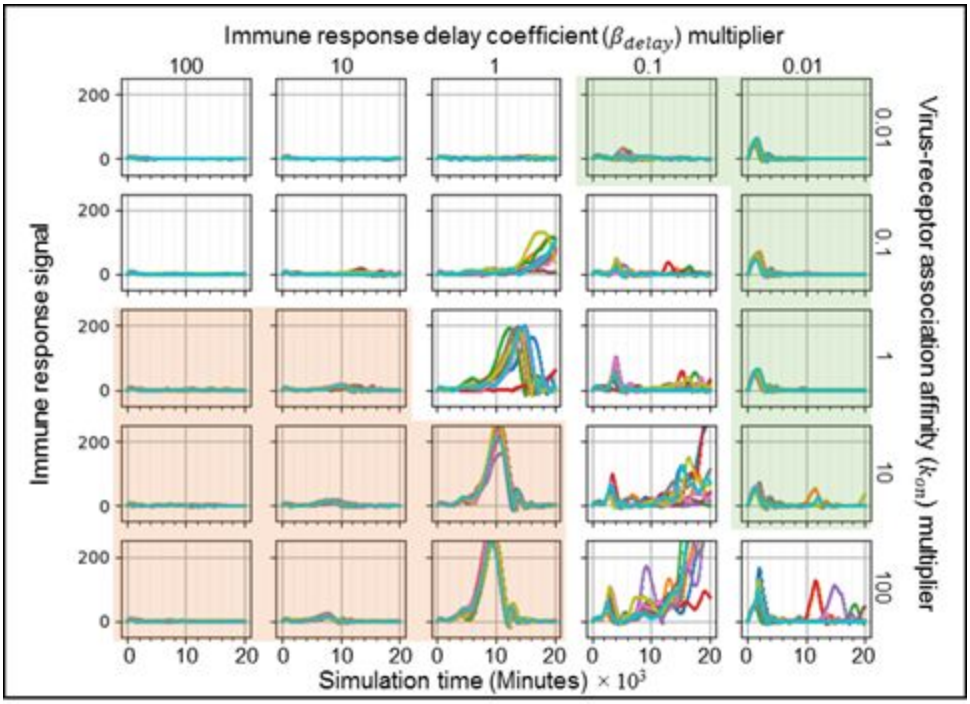

Figure S6. Time series of the immune response state variable S for simualtions in Figure 5. Logarithmic multidimensional parameter sweep performed by running 10 simulation replicas increasing and decreasing the baseline parameter values 10-fold and 100-fold for all parameter sets and replicas in Figure 5. Results show consistent containment/clearance for small k_{on} and small β_{delay} (upper right, green-shaded subplots), widespread infection for high k_{on} and smal β_{delay} (lower left, orange-shaded subplots), and multiple outcomes for some parameter sets (unshaded subplots). S is shown on a linear scale *vs* time in minutes.

Sweep of r_{max} multiplier and time delay of application

Dead cells

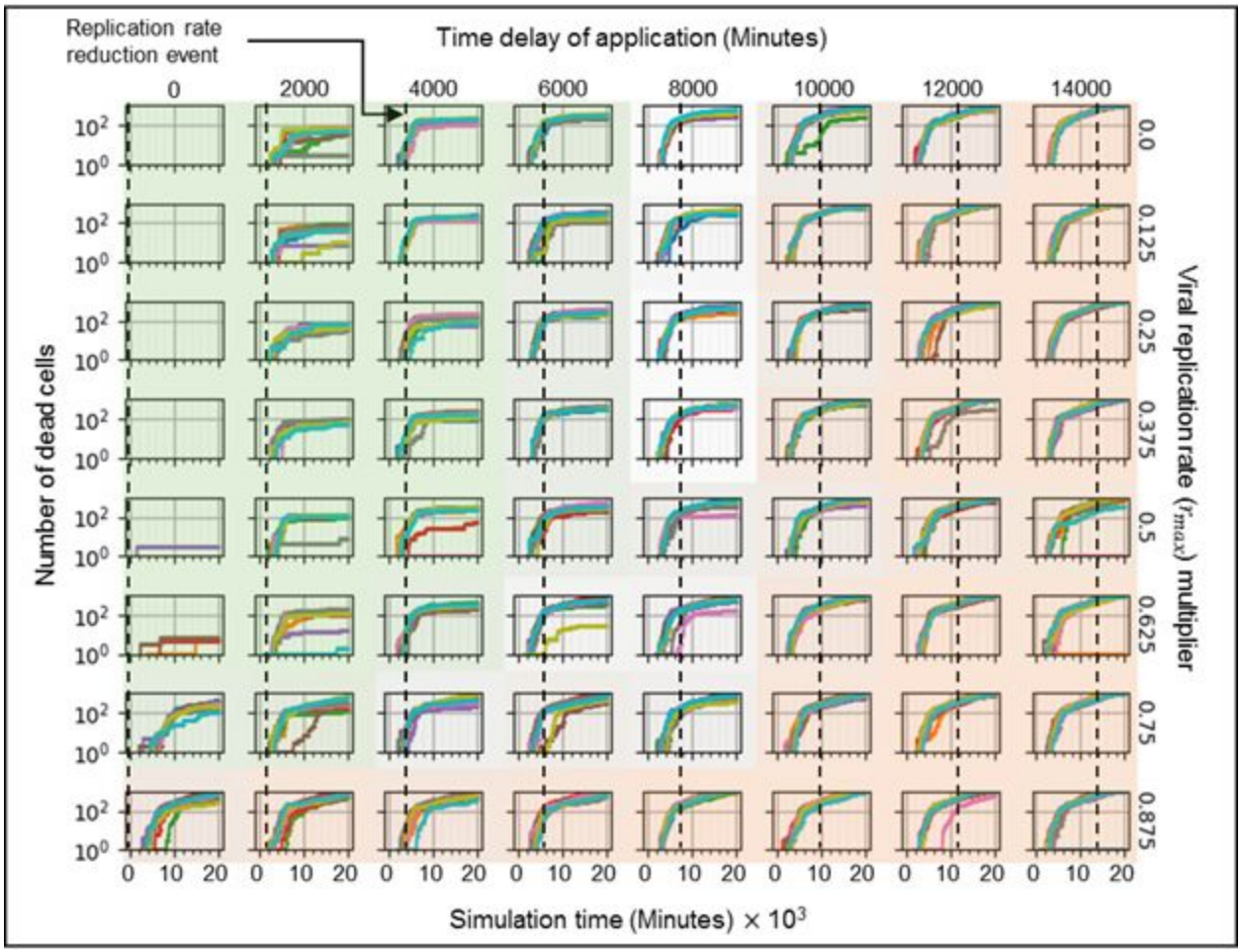

Figure S7. Simulations from Figure 8, showing the number of dead cells. Time series of the number of dead cells for each simulation replica in Figure 8. Number of cells is shown on a logarithmic scale *vs* time in minutes.

Infected cells

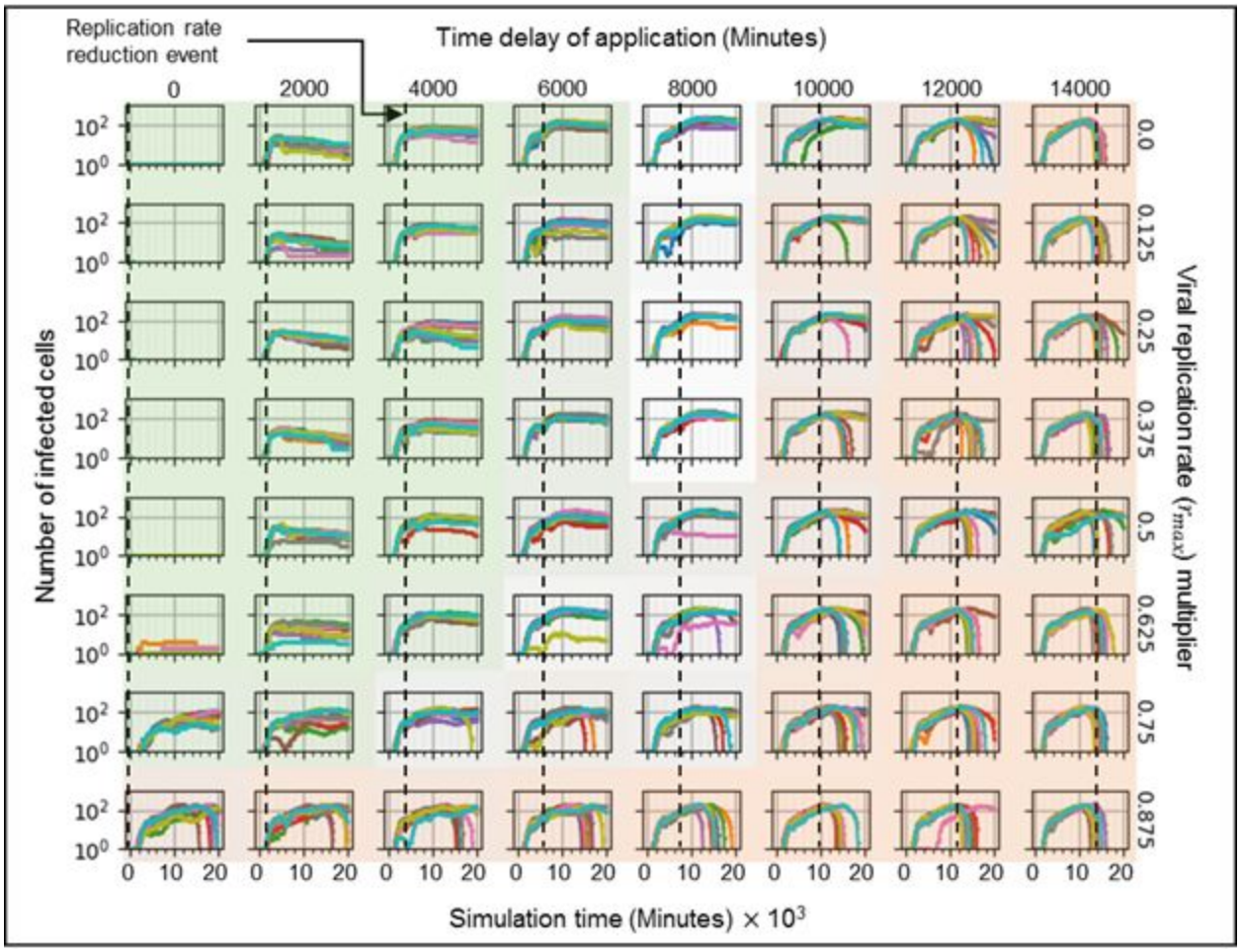

Figure S8. Simulations from Figure 8, showing the number of infected cells. Time series of the number of infected cells for each simulation replica in Figure 8. Number of cells is shown on a logarithmic scale *vs* time in minutes.

Immune cells

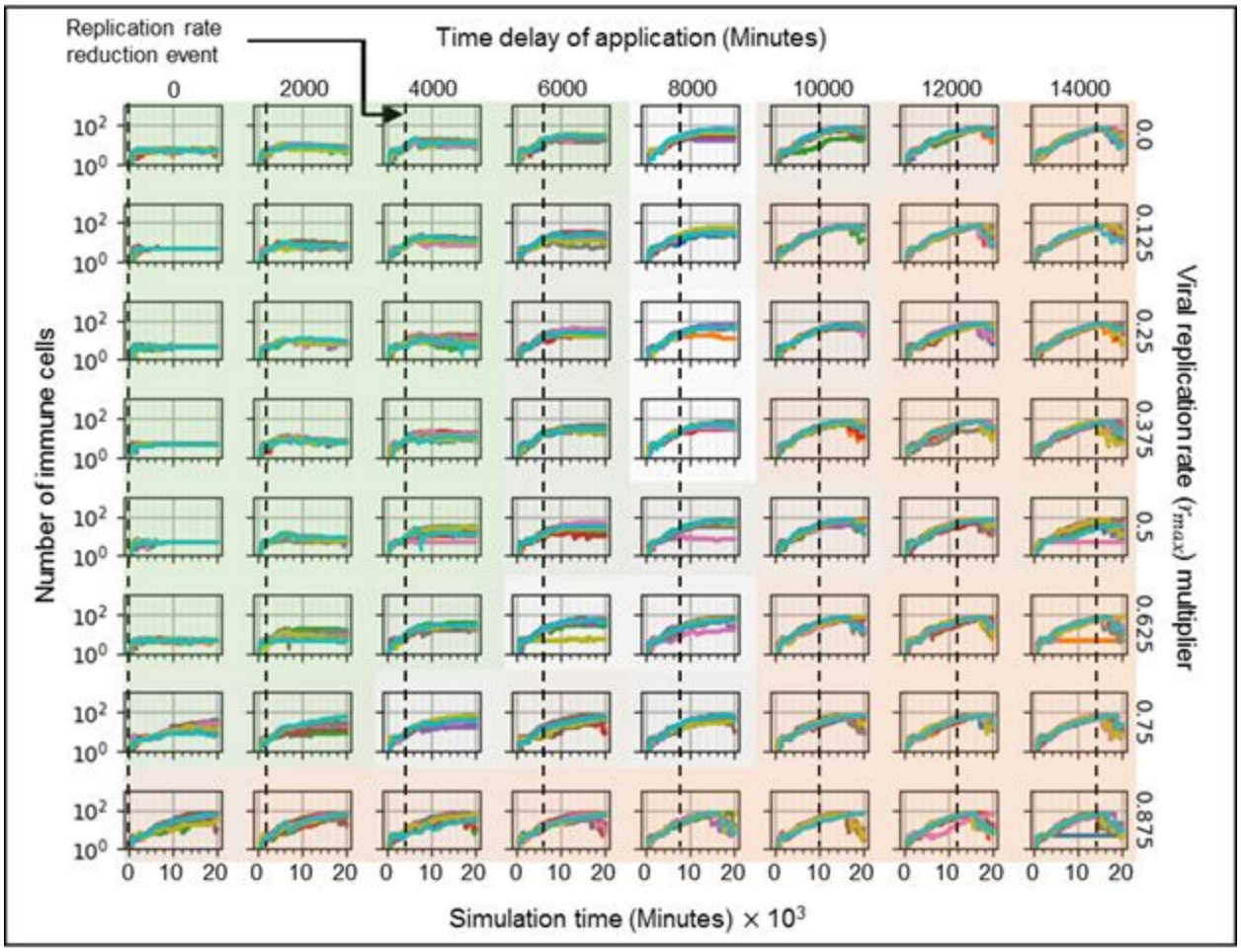

Figure S9. Simulations from Figure 8 showing the number of immune cells. Time series of the number of immune cells for each simulation replica in Figure 8. Number of cells is shown on a logarithmic scale *vs* time in minutes.

Immune response state variable

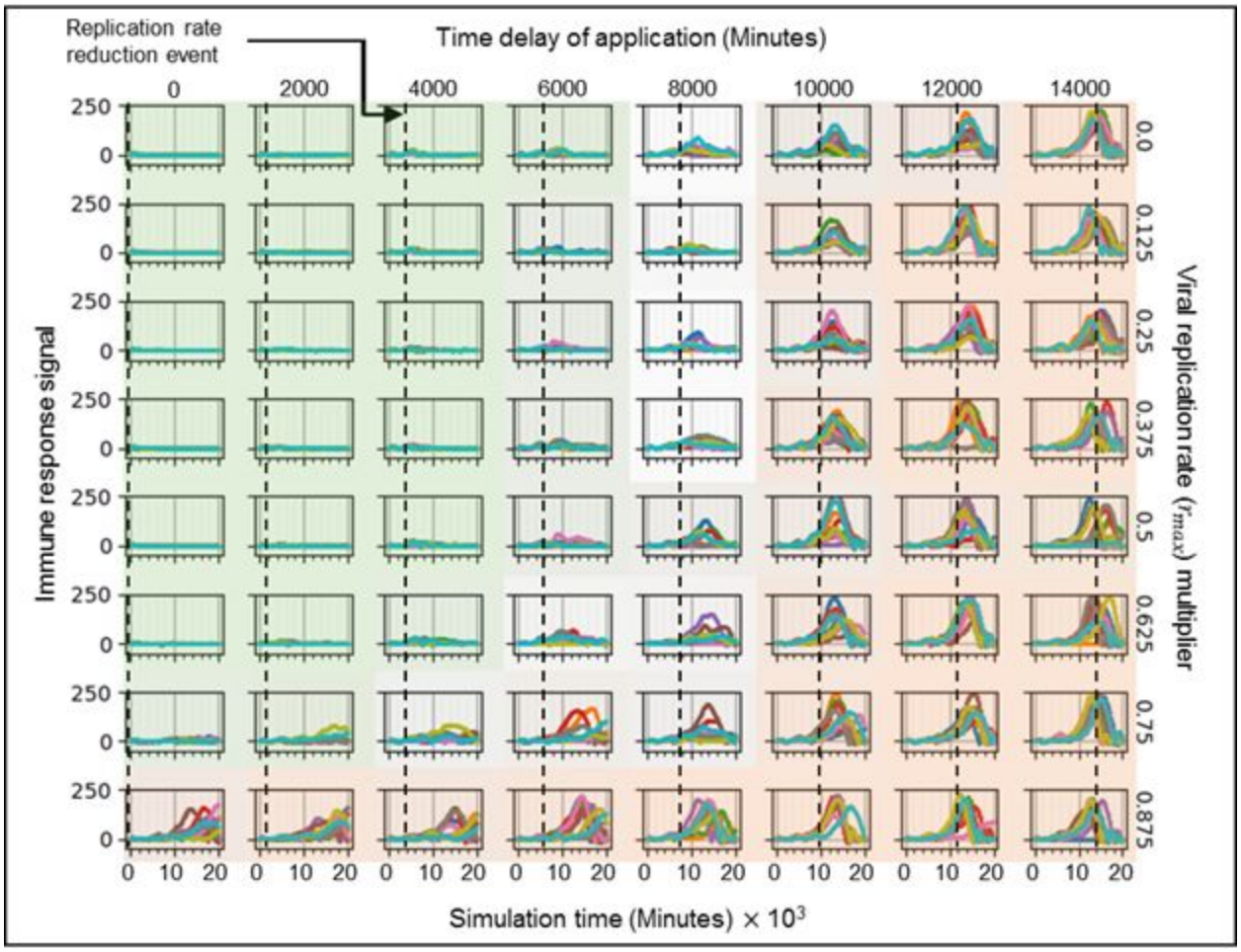

Figure S10. Simulations from Figure 8 showing the immune response state variable. Time series of the immune response state variable S for each simulation replica in Figure 8. S is shown on a linear scale *vs* time in minutes.

Variation in time delay of application about a bifurcation

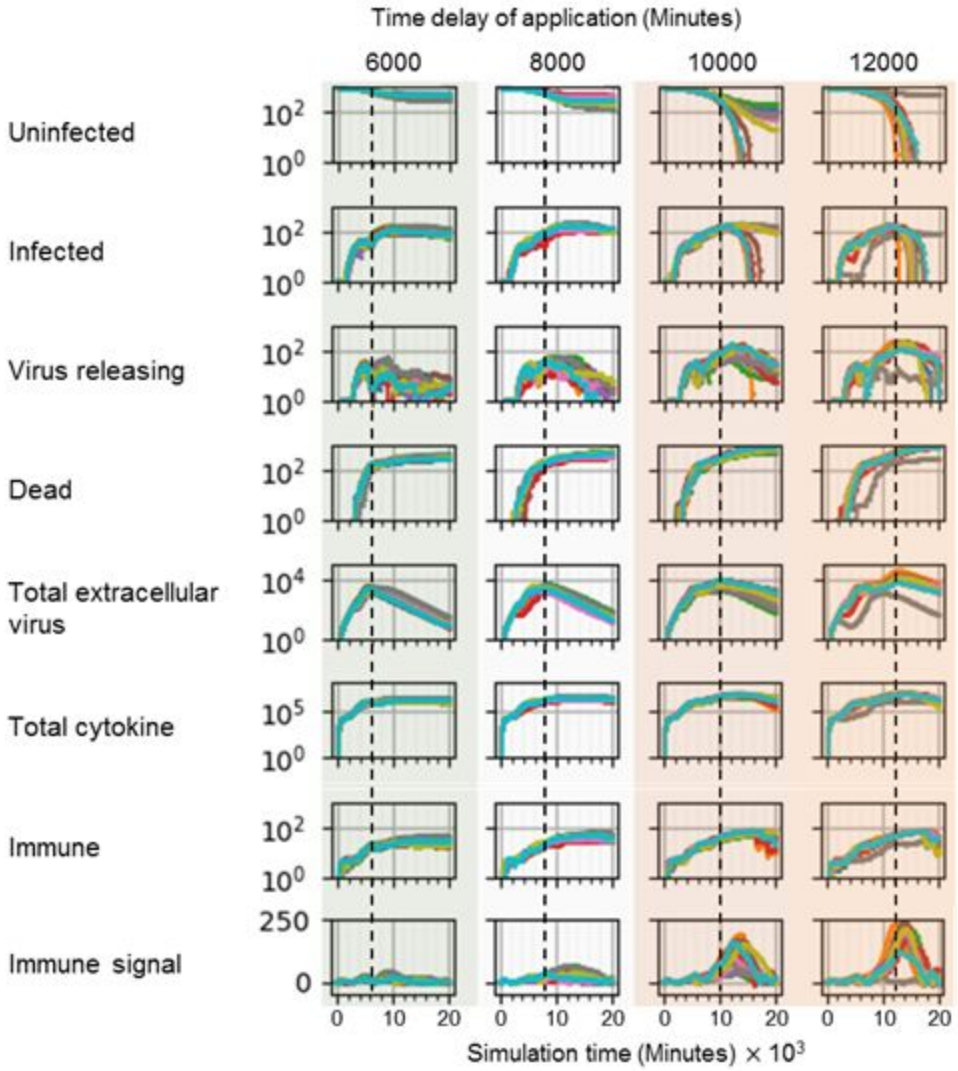

Figure S11. Variation in time of first treatment after infection with a reduced viral RNA replication rate causes a bifurcation in simulation outcomes. Simulations and parameters are as in Figures 9-11, for a viral replication rate multiplier of 0.375 and, from left to right, time delays of application of 6000, 8000, 10000, and 12000 minutes (100, 133, 167 and 200 hours, 4, 5 ½, 7 and 8 ⅓ days) (dashed lines). Results from all simulation replicas are shown vs time in minutes for, from top to bottom: number of uninfected cells, number of infected cells, number of virus releasing cells, number of dead cells, total extracellular virus, total cytokine, number of immune cells, and immune response state variable S. Parameter set subplots are shaded as in Figures 9-11 according to simulation outcomes.

Downloading and running the simulation

The COVID-19 simulation's source code is available in the GitHub repository https://github.com/covid-tissue-models/covid-tissue-response-models/tree/master/CC3D/Models

/BiocIU/SARSCoV2MultiscaleVTM. The simulation is a model specification which runs in the CompuCell3D virtual-tissue simulation environment. To run the simulation requires installation of CompuCell3D version 4.1.1 or later. CompuCell3D is open-source and runs on Windows, Mac and Linux operating systems. It can be downloaded from https://compucell3d.org/SrcBin. Installers are available for Windows operating systems and Mac installation also does not require compilation. CompuCell3D's manuals are available at https://compucell3d.org/Manuals. The COVID-19 simulation can also be run online without requiring any installations or downloads on the nanoHUB servers at https://nanohub.org/tools/cc3dcovid19/. Use of nanoHUB is free but requires user registration. The simulation may take a few moments to load in its nanoHUB deployment; during load the simulation area will be blue.

Twedit++ is a specialized text editor for CompuCell3D simulations which comes packaged with CompuCell3D. Tweedit++ can open *cc3d* file extensions which contain the simulation file structure for CompuCell3D simulations. To open the COVID-19 simulation click "Open CC3D Project" (Figure S12) and select *ViralInfectionVTM.cc3d* in `<repository-folder>/covid-tissue-response-models/CC3D/Models/BiocIU/SARSCoV2MultiscaleVTM/Model`. Once opened, *ViralInfectionVTM.cc3d* will appear in the left- hand panel "CC3D Simulation" (Figure S13). Double click on it to open all simulation files. The main simulation files are: *ViralInfectionVTM.xml*, which defines certain simulation properties (*e.g.*, cell types, lattice size, energy-constraint plugins, diffusive fields); *ViralInfectionVTMSteppables.py*, which defines the simulation's initial conditions, main interactions and dynamics (*e.g.*, cell initialization, immune-cell recruitment, secretion by cells into fields, uptake by cells from fields); *ViralInfectionVTMSteppableBasePy.py*, where the viral infection Antimony submodel is declared; *ViralInfectionVTMModelInputs.py*, which sets the parameters. The submodels in *ViralInfectionVTMSteppables.py* are organized as python classes, making them easy to modify. Tweedit++ can also copy and rename the simulation project to a new directory by using `CC3D Project; Save Project As`. However the save as does not copy the folder `<...>/Model/nCoVToolkit`, which must be copied into the new simulation directory separately.

CompuCell3D *Player* is a GUI tool which executes CompuCell3D simulations during desktop execution (or on nanoHUB). In order to run the simulation either right click *ViralInfectionVTM.cc3d* in the left hand panel and select "Open In Player" or open *CompuCell3D.exe* to open the CompuCell3D Player and select `File; Open Simulation File` and open *ViralInfectionVTM.cc3d*. Once the simulation is open in Player click play (on the nanoHub deployment the simulation should start automatically). Player will display windows with the cell lattice rendered (Figure S14), set the z-plane to 0 to visualize the epithelial cells and the z-plane to 1 to visualize the immune cells. More windows can be created (menu `Window; New graphics Window`, Figure S15) as needed to visualize the virus, cytokine, oxidative agent fields. Each window has a drop-down menu containing the selection of fields that can be rendered (*i.e.*, the chemical fields and the cell field, Figure S16).

Figure S12. Opening a CompuCell3D project in Tweedit++.

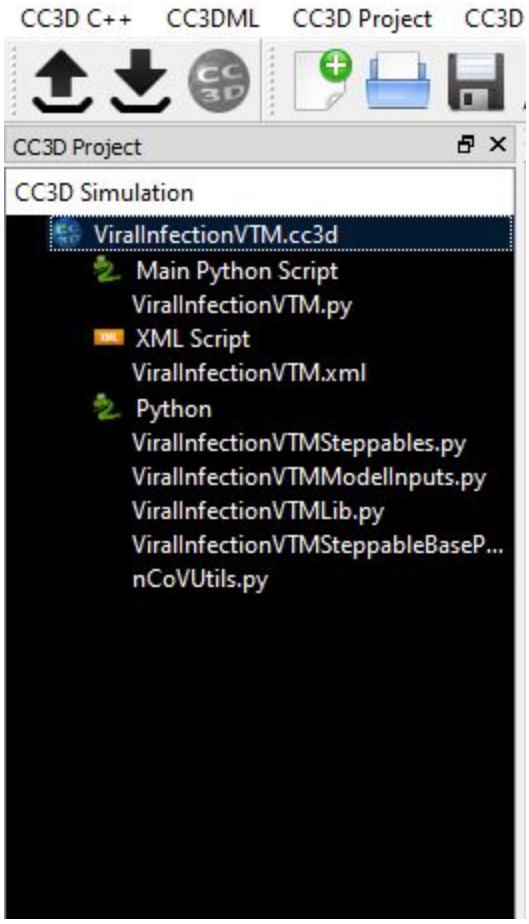

Figure S13. Tweedit++'s left hand panel with simulation project files openned.

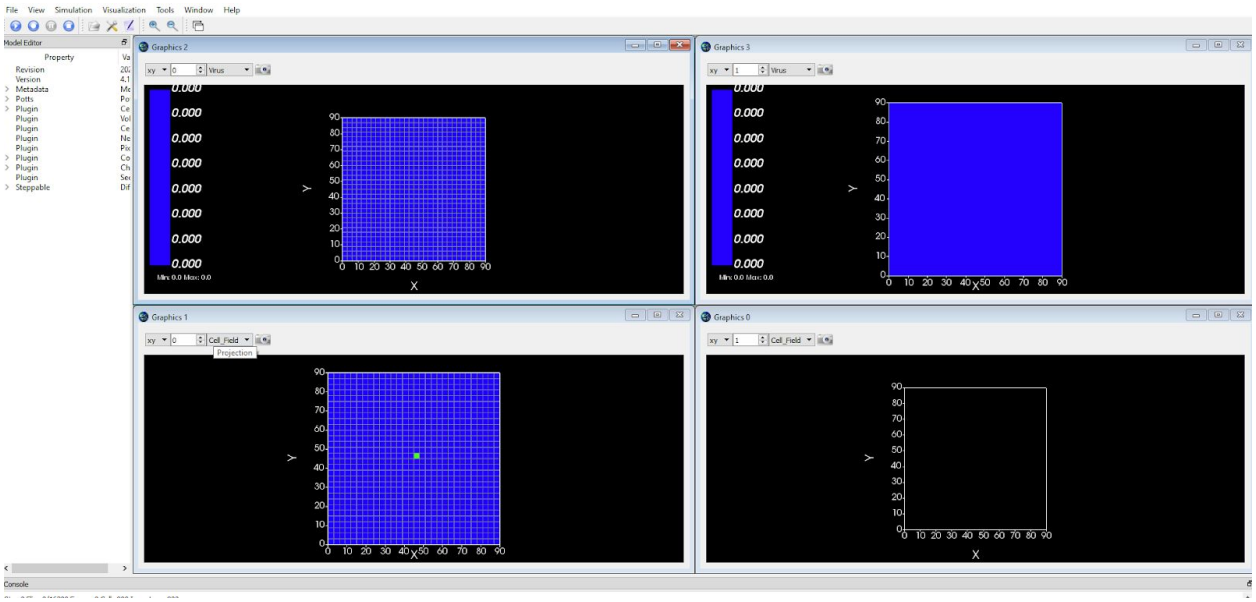

Figure S14. Example of CompuCell3D's player open with the COVID-19 simulation loaded.

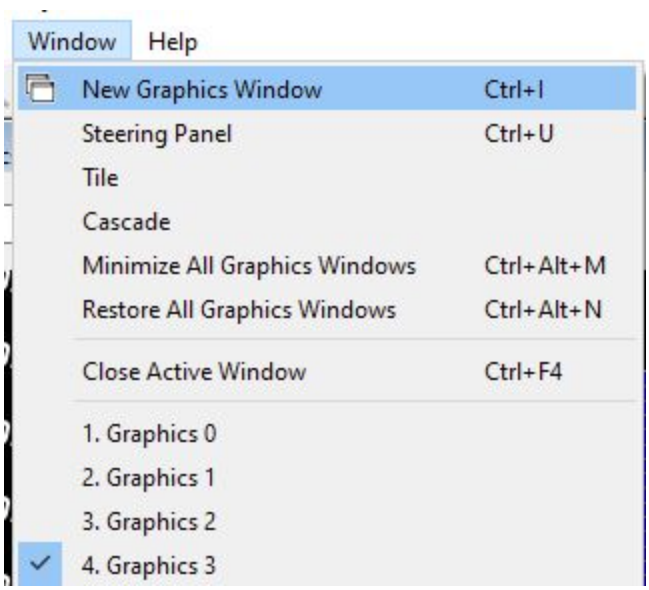

Figure S15. How to open a new simulation render window in CompuCell3D Player.

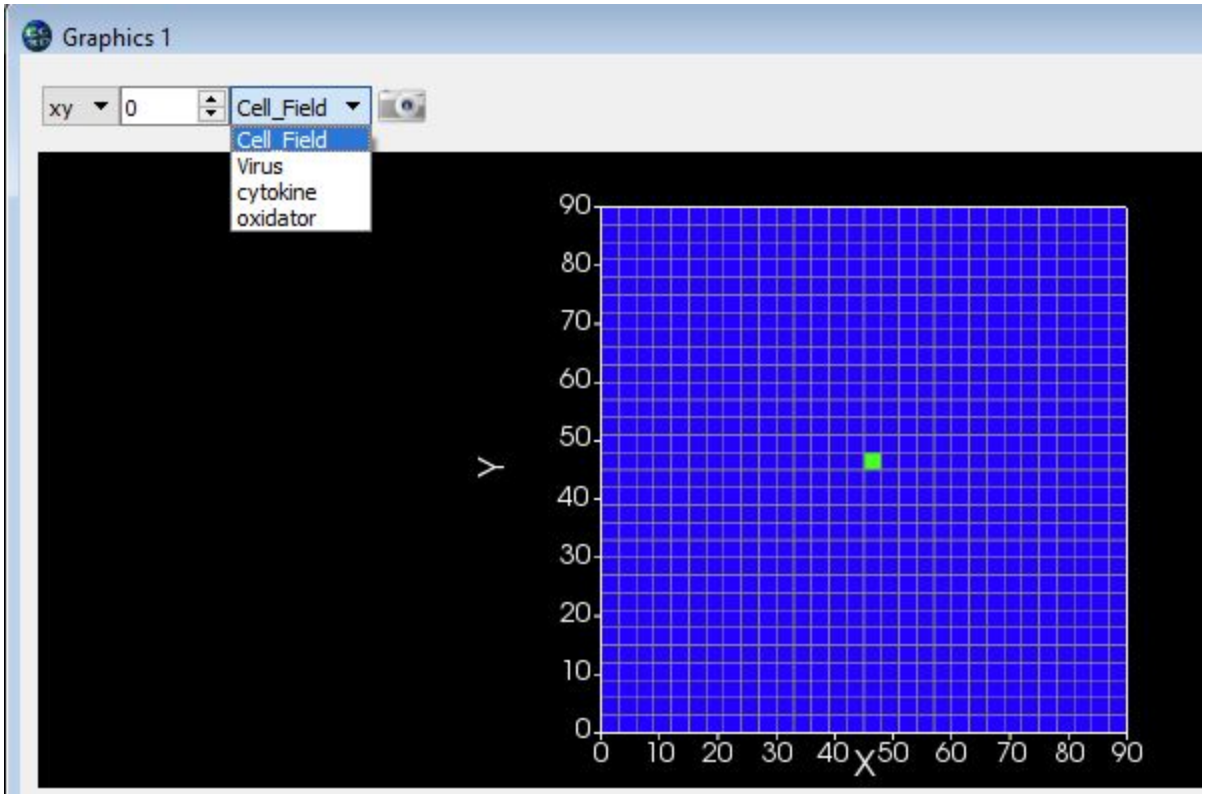

Figure S16. Drop-down menu in simulation render window to select which field to render.